You may also like:

Electrochemical Capacitors

Wide Bandgap Semiconductor-Based Electronics

Nanoengineered Separators for a High Energy Density, Long Cycle Life Li-S Battery
Weibing Xing

Gelatin methacryloyl and Laponite bioink for 3D bioprinted organotypic tumor modeling
Natan Roberto de Barros, Alejandro Gomez, Menekse Ermis et al.

In Operando Nanoscale Imaging for Lithium and Sodium Intercalation Compounds
Shirley Meng, Andrew Ulvestad, Oleg Shpyrko et al.

Chapter 7

Tailoring nanostructured fuel electrode materials for solid oxide cells through redox exsolution

Xiangling Yue and Shuai He

Fabricating solid oxide cell (SOC) electrodes (particularly their key components, such as electrocatalysts) at the nanoscale has generally been acknowledged to be advantageous for greatly extending their triple phase boundaries (TPBs), thus enhancing their performance and stability, diminishing interfacial reactions, allowing more diverse material choices, etc. It also has the potential to save materials and reduce operational costs. Various techniques used to introduce nanostructures have been addressed in other chapters of this book; these include atomic layer deposition (see chapter 5) and infiltration (see chapter 8). In this chapter, we focus on redox exsolution, which is a relatively new technique for creating nanomaterials in SOCs. We explain this concept, the fundamentals of its design, control of the evolving nanomaterials' microstructure and properties, and its applications in SOCs, followed by a summary of the advances in this strategy and its outlook for SOC development.

7.1 The concept of exsolution and its development

Exsolution is typically employed in materials that have an ABO_3 perovskite structure, which is well known for its flexibility in accommodating various dopants/valences within its lattice and its consequent versatility in modifying materials' structures, properties, and functionalities.

Exsolution refers to a method in which a catalytically active metal and/or metals, predominantly transitional metals, are doped into the crystal lattice of a parent oxide, forming a single-phase solid solution under oxidizing conditions (e.g. in air) and released as nanoclusters or particles on the surface of the oxide following extrinsic reduction, as shown in equations (7.1) and (7.2) and figure 7.1(a) [1], for example as a result of exposure to a H_2-containing atmosphere or the application of a cathodic potential.
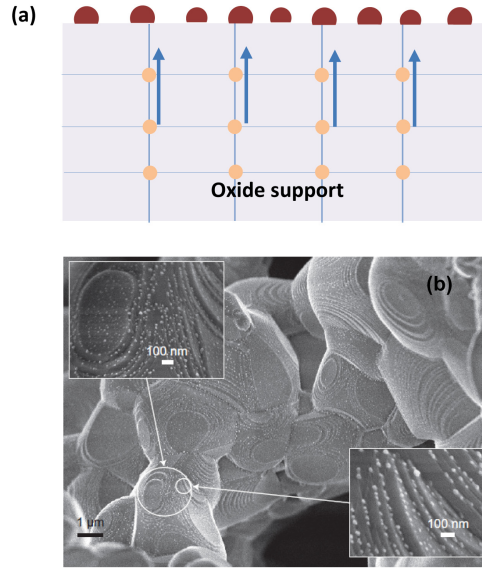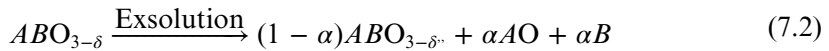
Figure 7.1. (a) Schematic of the exsolution phenomenon and (b) the exsolution-induced microstructure of a (La, Ce)(Ni, Ti)O$_3$ oxide material with prominent nanoparticles decorating the surface after reduction, whereas the surface was clean and smooth (free of nanofeatures) prior to reduction. Reproduced with permission from [2]. © University of St. Andrews and Dr Dragos Neagu.

$$A_{1-\alpha}BO_{3-\delta} \xrightarrow{\text{Exsolution}} (1-\alpha)ABO_{3-\delta'} + \alpha B \tag{7.1}$$

$$ABO_{3-\delta} \xrightarrow{\text{Exsolution}} (1-\alpha)ABO_{3-\delta''} + \alpha AO + \alpha B \tag{7.2}$$

Here, α stands for the extent of the A-site deficiency, which is an important factor that impacts the exsolution behavior of nanoparticles from a perovskite host (see section 7.3 for a detailed explanation).

The first step of the exsolution method is similar to the typical doping that is often used with perovskites to tune their properties. However, the choices of metal dopants as well as their reducibility in the following reduction treatment need to be considered during the materials design to ensure the formation of a single solid solution as well as the subsequent effective release of nanoparticles following reduction. From a microstructural point of view, these materials can be observed to have clean and nanofeature-free surfaces after the first step (i.e. before reduction); however, following reduction by either a reducing agent (such as H$_2$ or CO) or cathodic polarization, nanoparticles (or other types of nanostructure) can be seen decorating the surface of the supporting oxide, while the latter retains its perovskite structure. A schematic of the exsolution phenomenon and a typical microstructure generated by exsolution are displayed in figure 7.1. The numerous Ni nanoparticles in figure 7.1(b) were reported to be homogeneously distributed on the surface of La$_{0.8}$Ce$_{0.1}$Ni$_{0.4}$Ti$_{0.6}$O$_3$ after reduction in 5% H$_2$/Ar for 20 h at 930 °C [2].

The early concept of exsolution was reported in 2002 by Nishihata *et al*, who introduced the idea of the self-regeneration of precious catalyst particles, which helped to suppress particle growth in a three-way catalyst system for automotive emission control [3]. Pd particle aggregation and the resulting catalyst deactivation were severe problems in traditional Pd-impregnated γ-Al_2O_3 (Pd/alumina) catalyst systems. In Nishihata *et al*'s work, Pd was doped onto the *B*-site of a perovskite, forming a single-phase oxide, $LaFe_{0.57}Co_{0.38}Pd_{0.05}O_3$. When such a perovskite oxide was exposed to alternating oxidative and reductive environments at high temperature (900 °C)—conditions similar to the fluctuations in the redox characteristics of the automotive emission exhaust—it was discovered that Pd could reversibly move in and out of the perovskite structure, retaining its particle size at 1–3 nm, whereas impregnated Pd particles on the alumina support increased to 120 nm after 100 h. As a result, the Pd–perovskite catalyst maintained its high activity, but the Pd–alumina catalyst suffered from a performance deterioration of about 10% after an identical stability test. Due to the excellent lifetime performance demonstrated by the said self-regeneration process, $LaFe_{0.95}Pd_{0.05}O_3$ has been used as a commercial three-way catalyst for automotive emission control in gasoline engines ever since.

The approach was later extended to the incorporation of other precious-metal catalysts, such as Rh and Pt, within a wide range of perovskite compositions, including $CaTiO_3$, $SrTiO_3$, $LaAlO_3$, etc [4]. Although the extent of self-regeneration varied in different perovskite systems, it has generally been accepted that precious-metal-containing perovskite catalysts, also known as 'intelligent catalysts,' in which metallic clusters or nanoparticles emerge from the perovskite oxide upon reduction and dissolve back into the perovskite after oxidation, can successfully maintain a high level activity in prolonged cycled operations even at high temperatures. This technology, based on self-regeneration in a redox cycling environment, later known as redox exsolution, is an effective way of manufacturing highly active materials by careful design and selection of supporting oxide and metal catalyst, reducing the amount of precious-metal catalysts needed. It may thus solve the socioeconomic issues associated with the supply and demand of precious metals.

The success of these regenerative materials in catalysis attracted some attempts to apply the same methodology to the fabrication of solid oxide fuel cell (SOFC) electrodes. Using the exsolution concept, Barnett *et al* examined the capability of Ru, Pd, and Ni to dissolve into and precipitate out of an (La, Sr)CrO_3 oxide matrix and evaluated their performance as SOFC anodes [5–8]. It was reported that Ru could be incorporated into the chosen perovskite material and nucleated as metallic nanoclusters on the surfaces of oxide anodes at the initial reduction stage, which contributed to a continuous improvement in cell performance due to decreased anode polarization resistance for the first 300 h [5]. The precipitated Ru nanoclusters exhibited stable particle sizes of $\leq$5 nm for ~300 h and coarsened slightly over time up to 1000 h at 800 °C [7]. In addition, the outgrowth of bulk Ru from the perovskite and the corresponding anode performance were studied as functions of the dopant concentration and the reduction temperature [7]. The particle density increased following increased Ru concentration in the bulk at a given temperature, while

increasing the reduction temperature enlarged the size and decreased the population of the precipitated Ru nanoclusters.

It is worth noting that a nanoscale Ni catalyst was also produced through exsolution from a $La_{0.8}Sr_{0.2}Cr_{0.82}Ni_{0.18}O_{3-\delta}$ perovskite, yielding enhanced SOFC performance, which extended the applicability of the exsolution approach from precious-metal to Earth-abundant transition metals. However, the performance improvement was less pronounced compared to that of its Ru analog, which might coincide with the finding that the segregated Ni nanoclusters were much larger than the Ru (20 vs. 5 nm) variant and that the Ni nanocatalyst coarsened markedly, growing from 20 to 50 nm after being exposed to humidified H_2 for 311 h at 800 °C, whereas the Ru nanoclusters retained their size after an identical test [5].

At that time, the materials employing exsolution methodology investigated in the mainstream were confined to *A*-site stoichiometric perovskite compositions, which was concomitant with a small degree of nanoparticle exsolution, which gave rise to a limited population of nanocatalysts and hence insufficient fuel electro-oxidation activity at the SOFC anode.

The culmination of the exsolution concept has occurred in the last decade, when Irvine and Neagu *et al* extensively investigated titanate perovskites with the ability to grow numerous nanoparticles offering compositional diversity, including metals, oxides, and/or a mixture of the two on the surfaces of perovskites [1, 9–11]. By tuning the degree of non-stoichiometry (i.e. the deviation from the ideal ABO_3 stoichiometry) and varying compositions to tailor the surface characteristics of the parent oxide, dynamic exsolution of nanoparticles could be facilitated significantly, affording unprecedented control over particle size, distribution, and surface anchorage, particularly when *A*-site deficiency was adopted. Furthermore, they discovered the socketed nature of the exsolved particles with respect to their underlying perovskite support; in other words, the particles are deeply submerged into the perovskite with an epitaxial orientation. This strong interfacial interaction between the *in situ* grown nanoparticles and the oxide was believed to lead to a tremendously enhanced resistance against particle coarsening at elevated temperatures and coking in carbonaceous atmospheres and other functionalities to be explored.

Unlike the early studies of 'intelligent' catalysts, depending on the compositions of both the perovskite and the nanophase to be produced, the exsolved particles do not necessarily dissolve back into the perovskite matrix upon reoxidation, but are partly oxidized, retaining their anchorage to their supports at their initial location. This is particularly the case when *A*-site deficiency is adopted to boost the exsolution phenomena. The reason for this is the synergy between the *A*-site oxide and the segregation of the *B*-site metal. When an *A*-site deficiency is present, the precipitation of the *B*-site element is not accompanied by the formation of the *A*-site oxide on the surface, as occurs in the stoichiometric analog; thus, it is less likely for the *B*-site metal to revert back to the perovskite lattice with the dissolution of the *A*-site oxide and is more likely to lead to metal oxidation. Nevertheless, the oxidized nanophase can still possess superior catalytic activity or even provide new functionalities, as exemplified by NiCo alloy nanoparticles precipitated from $La_{0.7}Ce_{0.1}Ni_{0.3}Co_{0.1}Ti_{0.6}O_3$ [10]. In a CO oxidation reactor, the exsolved NiCo alloy oxidized following the light off

reaction conditions and reorganized its particles into tilted cube-like structures, which resulted in a nearly threefold increase in catalytic activity compared to the as-prepared NiCo metallic catalysts. Additionally, these NiCo cubes (with a particle size of 10 nm) exhibited doubled CO oxidation rates at high temperatures (>450 °C) and fivefold higher NO oxidation rates across the entire temperature range compared to the metallic state of the catalysts. The oxidized NiCo alloy cubes were demonstrated to rival a commercial Pt catalyst due to their remarkable catalytic activity and stability, which resulted from synergistic effects taking place at the cube–perovskite interface (which showed a semi-enclosed nanostructure), offering new pathways for the base metal oxide nanostructure to achieve Pt-like functionality.

Since the publication of this series of key findings, exsolution materials have been in the spotlight for catalysis and energy applications, including SOCs, and many researchers have joined this interesting area. The low P_{O2} environment in the fuel electrode compartment of SOCs is a good match for the conditions required to trigger the *in situ* exsolution of nanomaterials; therefore, SOCs can favorably take advantage of the operating conditions required to produce nanoscale electrode materials without any pretreatment, offering simplicity in manufacture together with excellent material activity and stability. Efforts have been made to validate the concept of exsolution in various fuel electrodes, covering a wide range of oxide materials, in order to enhance cell performance in fuel cell and/or electrolysis cell applications (see section 7.4). Success has been manifested in a wide array of perovskite systems, and the exsolved phases have offered compositional diversity as well. In contrast to the early studies, the vast majority of reports have addressed Earth-abundant base metal exsolutions, which are economically favorable considering the high cost and limited availability of noble metals.

7.2 Exsolution vs. infiltration

As an alternative technology for producing nanostructured SOC electrodes, exsolution has often been compared with infiltration, with respect to their surface morphologies, their interactions between the nanophase and the substrate, as well as their efficiencies in boosting the performance and stability of SOCs. As has been mentioned, it is well known that both technologies can produce diverse compositions and functionalities with nanofeatures, extending TPBs and consequently enhancing SOC performance compared to the traditional ceramic mechanical mixing approach. However, due to the striking difference in methodology, some outstanding phenomena have been generally acknowledged for each of these technologies, as will be discussed in the following.

As indicated in figure 7.1(a), exsolution is an inside-out method. The catalytically active component is first dissolved in the lattice of a host material, forming a solid solution—often under oxidizing conditions—and then grows on the surface as nanoparticles or nanoclusters; the latter typically takes place in a reducing atmosphere. In this way, the exsolved catalyst (regardless of its form, i.e. particles, cubes, rods, etc.) is coherently linked to the host perovskite at the interface, which is known as a socketed structure between the segregated nanophase and the parent
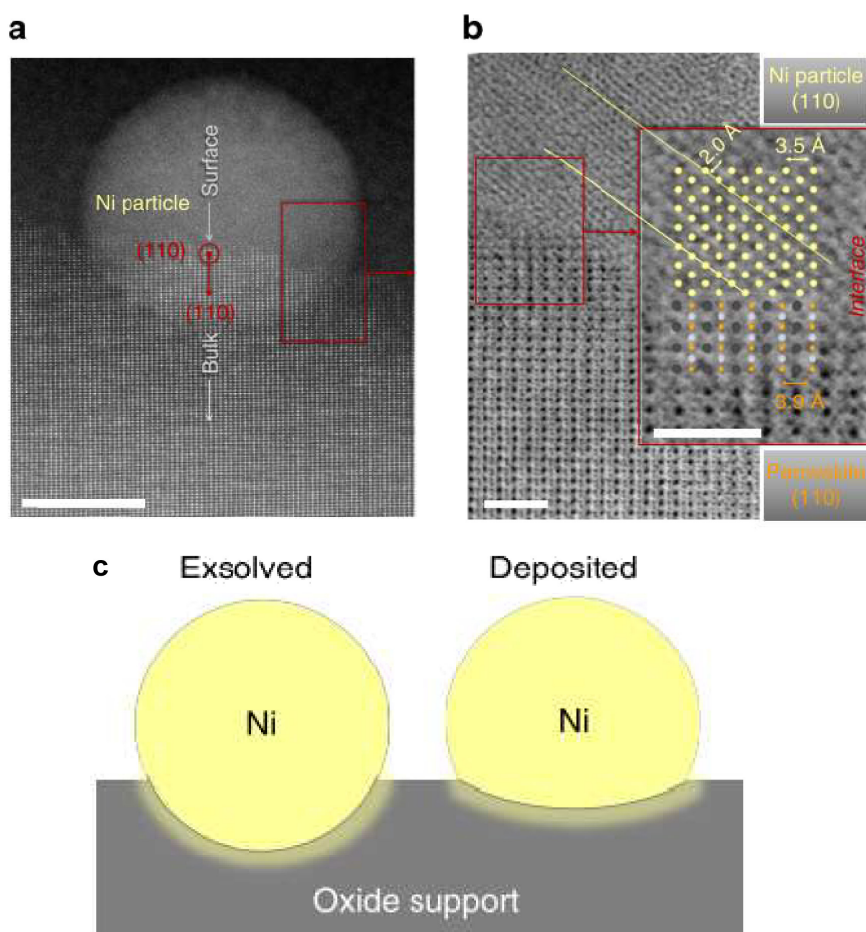
Figure 7.2. Transmission electron microscopy (TEM) micrograph of (a) a Ni particle exsolved from a (110) native surface facet of $La_{0.52}Sr_{0.28}Ni_{0.06}Ti_{0.94}O_3$ after ageing (3% H_2O 5% H_2/Ar, 900 °C, 60 h) and (b) the metal-perovskite interface highlighting the atomic planes and orientations after reduction (5%H_2/Ar, 900 °C, 12 h). (c) A schematic illustration of the interactions of exsolved and deposited Ni particles with the underlying support [9] Copyright © 2015, The Author(s). With permission of Springer.

oxide, as shown in figures 7.2(a) and (b). Infiltration is a fundamentally different method: nanoparticles are introduced by loading catalyst precursor solutions into a preformed porous solid support with the aid of capillary force and subsequent thermal treatment and reduction. When this approach is used, both the liquid–solid interactions between the catalyst precursor solution and the supporting scaffold as well as the subsequent solid–solid interactions after thermal treatment and reduction affect the interactions between the nanoparticles and their support.

Because of the intrinsically different procedures used for these two approaches, there are two crucial differences in the microstructure and morphology of the resultant nanofeatures. First, the distribution of nanoparticles and the particle size
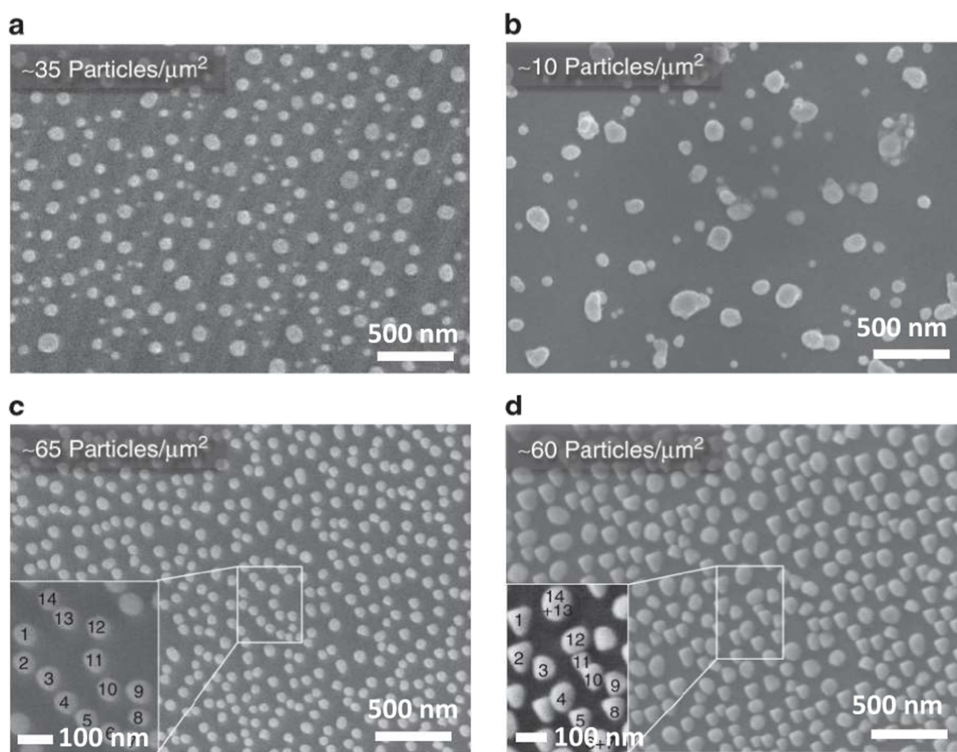
Figure 7.3. Comparison of deposited and exsolved Ni nanoparticles and their thermal stability. (a and b) SEM images of vapor-deposited Ni nanoparticles on $La_{0.4}Sr_{0.4}TiO_3$ (a) before and (b) after ageing (H_2, 650 °C, 24 h and 800 °C, 6 h); (c and d) SEM images of Ni particles exsolved from a $La_{0.52}Sr_{0.28}Ni_{0.06}Ti_{0.94}O_3$ (5% H_2/Ar, 900 °C, 12 h) cleaved surface (c) before and (d) after ageing (5% H_2/Ar, 900 °C, 70 h) [9] Copyright © 2015, The Author(s). With permission of Springer.

can be vastly contrasting. When infiltration is used, the distribution of the nano-phase is largely dependent on the structure of the porous scaffold/substrate and the properties associated with the precursor solution, such as its concentration, pH value, solvent type, chelating agent used, etc. which makes it complex to manipulate the distribution and the size of the nanoparticles [12]. When exsolution is used, the exsolved phase initially forms a single solid solution within the framework of the support; when the environment is altered, metal cations diffuse from the bulk to the surface of the support and become reduced, decorating the surface with a metallic or oxide nanophase (or even a mixture), leading to a more homogeneous coverage of nanofeatures, as demonstrated in figure 7.3 where the microstructures of deposited and exsolved Ni nanoparticles are compared. Note that not only the coverage but also the particle density, size, and shape can also be conveniently controlled by altering the initial doping concentration, reduction temperature, P_{O2}, or non-stoichiometry in the parent oxide composition in exsolution (see section 7.3).

Second, the attachment of the nanoparticles (or other forms) to their support is tremendously distinct in the exsolution compared to that in infiltration processing.

This attachment is a key factor impacting the morphology and microstructural evolution during ageing and long-term operation. It is well known that the infiltrated nanoparticles are weakly attached to their support, which was validated in an experiment in which shallow pits remained in an infiltrated system after the catalyst was etched away by diluted nitric acid [9]. Due to this weak interaction, the infiltrated nanoparticles tend to agglomerate easily at high temperatures and in prolonged operations. Figures 7.3(a) and (b) aptly display the microstructural evolution one could expect from infiltrated/impregnated nanoparticles subjected to an ageing test, although these nanoparticles were obtained by vapor deposition, which has similar issues. The growth and coalescence of nanoparticles would negate the benefits of the nanostructure due to a reduction in surface area and the active sites available for catalytic reactions, leading to inevitable performance degradation, which is the greatest obstacle to infiltration technology.

In contrast, exsolved nanoparticles are deeply embedded into the substrate, as they grow from the perovskite lattice (figures 7.1(a) and 7.2) by diffusion through the bulk to the surface and nucleation on the surface following reduction. In fact, an epitaxial growth of exsolved Ni particles along the interface was observed by electron diffraction, as exhibited previously in figure 7.2(b). These strong interactions endow the exsolved nanoparticles with excellent thermal stability against ageing. As demonstrated in figures 7.3(c) and (d), the Ni nanoparticles precipitated via the exsolution route grew only slightly during a 70 h ageing test at 900 °C, and their particle density was almost unchanged; their deposited Ni counterparts, on the contrary, experienced a considerable growth in particle size and hence a significant loss of particle density in a similar ageing test at an even lower temperature, i.e. 800 °C (figures 7.3(a) and (b)). The stronger attachment of the exsolved particles to the support was also evidenced by the much deeper pits in the exsolved materials than those of the infiltrated materials after the nanoparticles were removed in a similar etching experiment [9]. This contrast in the extent of the interactions between the nanoparticles and their substrates in the two systems, i.e. exsolution and infiltration, is also schematically illustrated in figure 7.2(c), which makes it easier to understand/interpret the striking difference in the performance and stability of SOC electrodes fabricated by infiltration and exsolution. The stronger interactions between nanoparticle and the substrate are clearly beneficial for increasing the robustness of the system as well as maintaining high performance, reducing the long-term operational cost of SOCs.

Furthermore, it has been found that the stronger interfacial interactions in the exsolution materials disrupted the carbon fiber growth mechanism, leading to completely different coking behavior compared to the infiltrated or deposited nanocatalyst system. As depicted in figure 7.4, the growth of carbon fiber in the infiltrated or deposited Ni catalyst system was believed to follow a tip-growth mechanism, in which the Ni catalyst was lifted by carbon fiber forming underneath it due to the weak interaction between the Ni catalyst and its support, which prompted the growth and accumulation of lengthy fibers, as seen in figure 7.5(a). However, in the exsolved system, the growth of fiber was massively inhibited because the Ni nanocatalyst was deeply embedded in the support,
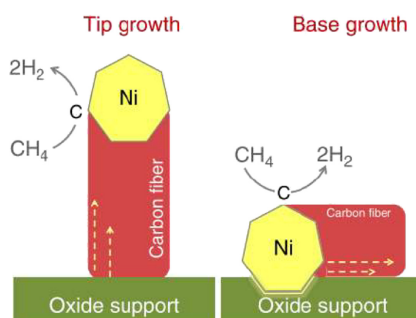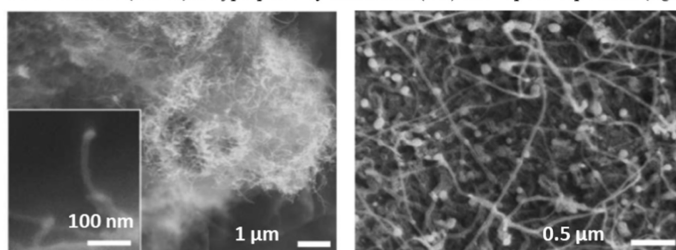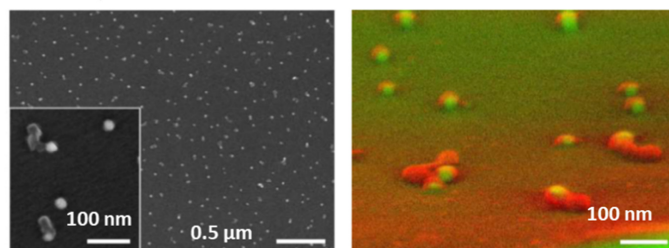
Figure 7.4. Illustration of the possible carbon fiber growth mechanisms of infiltrated (left) and exsolved (right) Ni nanoparticles [9] Copyright © 2015, The Author(s). With permission of Springer.
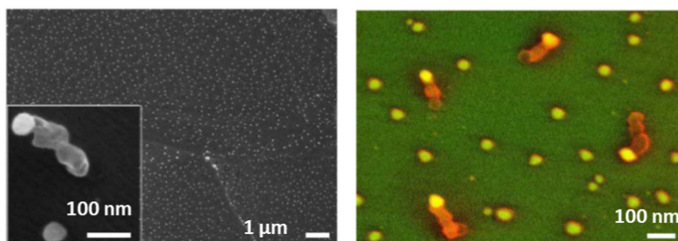

Figure 7.5. SEM micrographs of (La, Sr)$_{0.8}$TiO$_3$ with Ni nanoparticles prepared via different routes and conditions after identical coking tests (20% CH$_4$/H$_2$ at 800 °C, 4 h) (red denotes carbon and yellow represents Ni in the false-color images in b and c; adapted) [9] Copyright © 2015, The Author(s). With permission of Springer.

rendering it hard to be lifted by carbon fiber grown underneath, hence a base growth mechanism was favored. In the base growth scenario, very short carbon fibers were found beside the Ni nanoparticles, as can be observed in figures 7.5(b) and (c) where negligible coking occurred on the surface of the (La, Sr)(Ni, Ti)O_3 material after a coking test in 20% CH_4/H_2 at 800 °C for 4 h. In conclusion, the exsolved catalyst displayed remarkable coking resistance and hence experienced only minor coking due to the strong particle–support interaction, while the impregnated catalyst suffered from severe carbon formation by virtue of the weak interaction between the catalyst and the support.

Another characteristic of exsolution materials is their superior sulfur tolerance, which results from the strong interactions between the exsolved particles and their support. When compared with a commercial Ni/Al_2O_3–SiO_2 catalyst, both the exsolved Ni/$La_{0.8}Ce_{0.1}Ni_{0.4}Ti_{0.6}O_3$ and Ni–Fe/$La_{0.5}Sr_{0.4}Ni_{0.1}Fe_{0.1}Ti_{0.8}O_3$ materials showed better tolerance to sulfur poisoning after sequential exposure to 50 ppm of SO_2 gas for 15, 30, and 60 min; the Ni–Fe decorated system demonstrated no change in catalytic activity for CO oxidation after the sulfur poisoning experiment [13]. High H_2S tolerance and sustained stability was also demonstrated for *in situ* exsolved NiCo alloy nanoparticles anchored on a Ruddlesden–Popper support when up to 100 ppm of H_2S was introduced into the CO/CO_2 fuel mixture used for CO_2 electrolysis [14].

In summary, exsolution materials, due to their unique interactions between the exsolved nanoparticles and the support, offer exceptional catalytic activity and stability, new functionalities, and more to be explored. From the point of view of SOC performance and stability, exsolution does seem to offer a number of advantages over infiltration, such as higher resistance to particle coalescence, carbon deposition, and sulfur attacking. From the perspective of manufacture, infiltration can be troublesome, as the process needs to be repeated to meet the required mass loading and it offers less control over particle size and distribution, while exsolution can rather simply take advantage of the SOC operating conditions to complete the reduction necessary to generate nanoparticles and can manipulate the particle size and population by tailoring the reduction conditions. Yet, there are other considerations and limitations related to materials design and SOC fabrication and application. There are apparently more options for catalysts in the infiltration method so long as the catalyst is chemically and thermochemically compatible with the support, whereas the options for the exsolution approach are confined to catalysts that can be dissolved into the support lattice structure and easily reduced and grown on the surface upon reduction. In addition, the bulk properties of the support, such as its conductivity, can be dramatically altered by the dopant, doping level, and perovskite support used in the exsolution strategy, while in the case of the infiltration strategy, the bulk properties are often dictated by the scaffold, which is not significantly impacted by the impregnates and their concentrations. Given the differences between infiltration and exsolution, there are possible synergies between these two approaches that may combine their respective advantages [15]. However, this has not been investigated extensively.

7.3 Tailoring material morphologies and functionalities through exsolution

It is essential to understand the mechanisms of the exsolution phenomenon, such as the fundamentals and driving forces of such an intriguing process. Such an understanding provides the insights and general guidance required to tailor materials' properties, morphologies, and functionalities for practical applications through exsolution. In the following sections, the exsolution thermodynamics and driving forces that have been generally accepted will be discussed first, followed by an introduction to the factors that have been proven effective for tuning the exsolution of nanoparticles.

7.3.1 The thermodynamics and driving forces of exsolution

From a thermodynamic point of view, the exsolution of a metal (M) is governed by its Gibbs free energy change (ΔG) from M^{n+} to M^0 during reduction, which acts as the main driving force for exsolution (see equation 7.3). Figure 7.6 shows the $\Delta G_{red.}^{900}$ of reduction of oxides to either metals or selected oxides at 900 °C in H_2 [2]. According to the figure, certain metals that are known to have the exsolution capability exhibit $\Delta G_{red.}^{900} < 0$, e.g. Fe, Co, Ni, Cu, and noble metals. This means that from a theoretical perspective, the reduction of these metal cations is thermodynamically favored and spontaneous at 900 °C. Conversely, in the cases of Ti, Mn, and Zn, positive $\Delta G_{red.}^{900}$ is seen, indicating unfavorable reduction or exsolution.
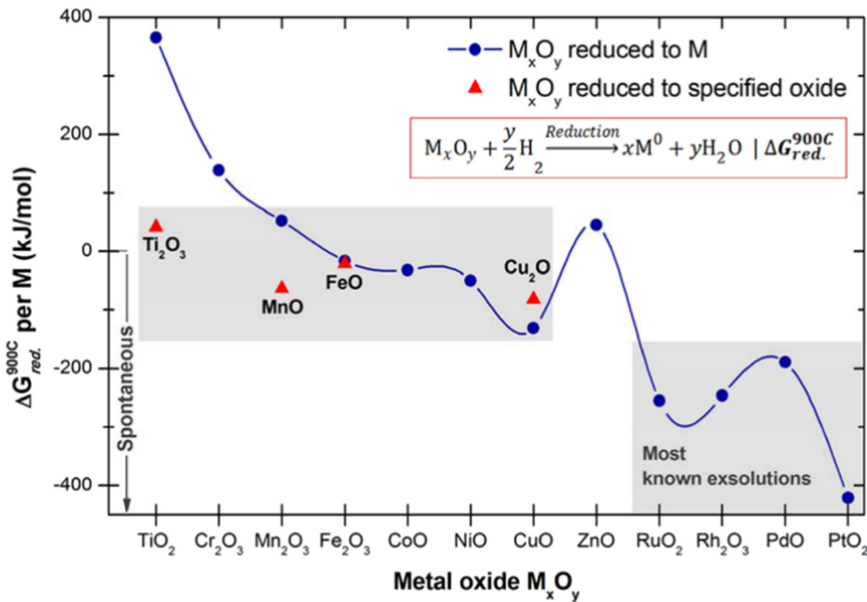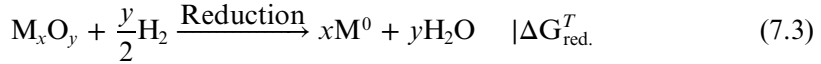

Figure 7.6. The Gibbs free energy of the reduction of oxides to either metals or selected oxides at 900 °C in H_2. Reproduced with permission from [2]. © University of St. Andrews and Dr Dragos Neagu.

$$M_xO_y + \frac{y}{2}H_2 \xrightarrow{\text{Reduction}} xM^0 + yH_2O \quad |\Delta G_{red.}^T \quad (7.3)$$

The Gibbs free energy of reduction $\Delta G_{red.}^T$ of a metal only serves as a primitive guide for predicting the phenomenon of exsolution and comparing the exsolution capabilities of different metals. In realistic exsolution systems, the ability of a metal to exsolve is complicated and can be influenced by different factors. As mentioned earlier, it has been accepted that exsolution comprises several processes, namely cation diffusion, reduction, nucleation, and growth, as indicated in figure 7.7 [16]. Figure 7.8 describes the Gibbs free energy change during nucleation and growth. According to the classical isothermal nucleation theory, nucleation is related to the ΔG of the nucleus at the critical particle size (r^*), i.e. the critical free energy (ΔG^*), which can be expressed as follows:

$$\Delta G^* = \Delta G_{bulk}^* + \Delta G_{interface}^* + \Delta G_{surface}^*, \quad (7.4)$$

where the terms on the right-hand side of the equation denote the ΔG^* of bulk reduction, that of the newly formed metal/perovskite interface, and that of the metal surface, respectively. These values are system- and temperature-dependent, and the latter two terms are highly relevant to the surface morphology. For example, in a Ni exsolution system $La_{0.43}Sr_{0.37}Ni_{0.06}Ti_{0.94}O_{3-\delta}$ (LSNT), Ni^{2+} cations diffuse from the bulk to the surface of the material and are subsequently reduced to Ni^0 metal. The reduced nuclei assemble into small nanoparticles, which grow in size with reduction time and temperature [16]. From the exsolving material's perspective, the extent of its exsolution is determined by the surface/bulk mechanical energy (the strain effect)
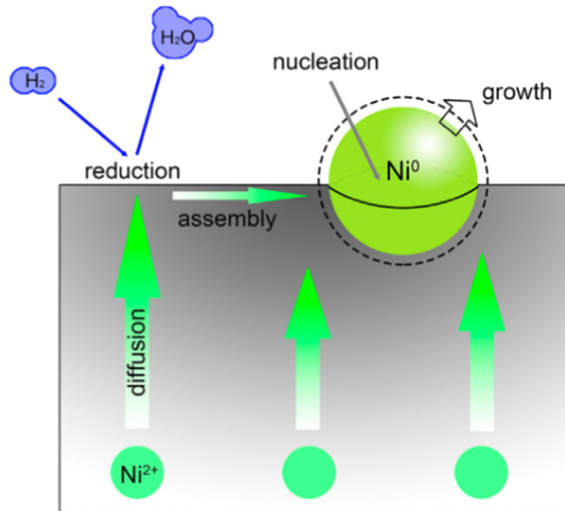

Figure 7.7. A scheme of the exsolution process: Ni cations in the perovskite lattice first diffuse to the surface and are subsequently reduced to Ni^0 metal; the particle size increases as a function of time and temperature. Reprinted from [16], Copyright (2016), with permission from Elsevier.
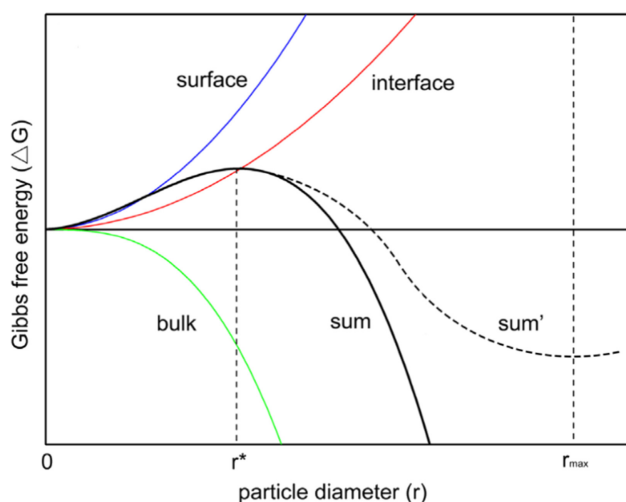
Figure 7.8. Gibbs free energy change during nucleation and growth. Reprinted from [16], Copyright (2016), with permission from Elsevier.

and the metal cation supply and cation diffusion rate, which can be influenced by many intrinsic and extrinsic factors (see below for a detailed discussion).

In principle, the exsolution of nanoparticles is driven by the gradient of the exsolving species across the material bulk to the surface, which can be controlled and promoted in various ways, for instance by material composition, defect chemistry (e.g. non-stoichiometry and lattice defects), surface features, oxygen partial pressure (P_{O2}), temperature/time, electrochemical bias, strain, light, etc. Neagu *et al* introduced *A*-site deficiency ($\alpha = 0.2$) into a $La_{0.52}Sr_{0.28}Ni_{0.06}Ti_{0.94}O_3$ titanate and observed a significant promotion of nanoparticle exsolution compared to its *A*-site stoichiometric counterpart [1]. Han *et al* grew $La_{0.2}Sr_{0.7}Ni_{0.1}Ti_{0.9}O_{3-\delta}$ thin films on various lattice-mismatched substrates, which induced different degrees of lattice misfit strain [17]. Compressive-strained films showed a larger number of exsolved particles than tensile-strained films, eventually reaching more than 1100 particles/ μm^2 with a particle size as small as ~5 nm via strain control. Myung *et al* applied an electrolysis voltage (~2 V) to a SOC electrode made from $La_{0.43}Ca_{0.37}Ni_{0.06}Ti_{0.94}O_{3-\delta}$ and found that such an electrical reduction remarkably facilitated Ni exsolution (~a few minutes) compared to chemical reduction (~tens of hours) [18].

One fascinating aspect of exsolution is that the final exsolved structure can be controlled and adjusted by sophisticated material design and the subsequent treatment. In the following sections, the typical controlling factors used to drive exsolution and determine materials' morphologies will be introduced.

7.3.2 Controlling factors for the exsolution process

Since the exsolution strategy facilitates a broad range of functional applications in the field of catalysis and electrocatalysis, it is important to identify the respective

factors that control and determine the properties of exsolved nanoparticles. As mentioned earlier, factors such as stoichiometry, the surface characteristics of the parent material, oxygen partial pressure, electrochemical bias, etc. have been found very effective in influencing exsolution behavior. In this section, we discuss the mechanisms responsible for the methods commonly utilized to tune the exsolution process, and typical examples are given where necessary.

7.3.2.1 Stoichiometry

The stoichiometry of a perovskite plays a crucial role as an intrinsic factor in controlling and tailoring the exsolution. The general stoichiometry of perovskite oxides is ABO_3; this conventionally possesses a large cation at the A-site and a smaller cation at the B-site. By adjusting a stoichiometric perovskite to be a non-stoichiometric one, its exsolution behavior can be vastly altered. In the ABO_3 framework, non-stoichiometry or defects can take the form of A-site deficiency/excess, B-site deficiency/excess, or oxygen deficiency/excess. Among these, A-site deficiency has been most frequently used to promote exsolution and has been regarded highly effective.

Unlike the exsolution that occurs in near-stoichiometric perovskites, the pioneering study by Neagu *et al* demonstrated that A-site deficiency ($A/B = (1-x)/1$) plays a crucial role in boosting B-site exsolution, thus facilitating the production of large quantities of embedded nanoparticles [1]. Figure 7.9 shows that significant numbers of Ni nanoparticles were exsolved from an A-site deficient $La_{0.52}Sr_{0.28}Ni_{0.06}Ti_{0.94}O_3$ backbone after reduction, while no exsolution was observed from A-site stoichiometric $La_{0.3}Sr_{0.7}Ni_{0.06}Ti_{0.94}O_{3.09}$.

One possible mechanism for the beneficial effect of A-site deficiency is that upon creating A-site deficiency in a perovskite ($A_{1-x}BO_3$), a large number of oxygen vacancies are generated. To retain the balance of charges and equilibrium, the perovskite lattice tends to release the local 'excess' of B-site cations. Upon reduction, the excess B-site cations are driven across the perovskite lattice by its gradient and diffuse to the surface. This process is also accelerated by the oxygen partial pressure

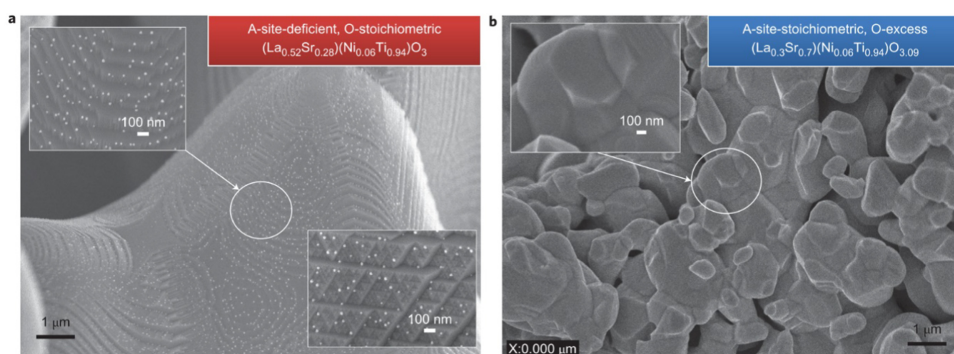**Figure 7.9.** SEM micrographs showing (a) exsolution from initially A-site deficient $La_{0.52}Sr_{0.28}Ni_{0.06}Ti_{0.94}O_3$ and (b) A-site stoichiometric $La_{0.3}Sr_{0.7}Ni_{0.06}Ti_{0.94}O_{3.09}$ after reduction at 930 °C for 20 h in 5% H_2/Ar [2]. Reproduced with permission from [2]. © University of St. Andrews and Dr Dragos Neagu.

gradient. The diffused BO_x is reduced to metallic B and grows as exsolved nanoparticles. Therefore, the stoichiometry of the A-site deficient perovskite after exsolution approaches $ABO_{3-\delta}$, which is more thermodynamically stable (see equation (7.1)). Since the perovskite is already A-site deficient, the formation of AO (oxide) upon exsolution is unlikely to occur.

To date, introducing A-site deficiency into the material structure has been extensively employed for various perovskite oxide systems. For example, the A-site deficient transition-metal-doped titanates (e.g. $(La, Sr)_{1-\alpha}Ti_{1-x}M_xO_{3-\delta}$, M = Fe, Co, Ni, Cu, Mn, etc.) clearly benefit in terms of the degree of exsolution, compared to the A-site stoichiometric design [19–23].

7.3.2.2 Surfaces

Solid materials interact with their surroundings through surfaces. The physical and chemical compositions of these surfaces determine the nature of the interactions. Therefore, surfaces influence many crucial properties of the material. *In situ* exsolution is practically a surface phenomenon; the first layers of atoms at the top surface interact with the reducing media, providing a driving force for cation diffusion, nucleation, and growth. The attributes of exsolved nanoparticles are largely influenced by the surface properties; therefore, this section discusses the impact of different surface characteristics on nanoparticles' exsolution behavior.

The surfaces of a material right after its fabrication (e.g. by calcination), without further treatments, are regarded as native surfaces. Reports suggest that the stoichiometry of a perovskite's native surface is not necessarily identical to that of the bulk. Surface A-site enrichment in perovskites has been reported on numerous occasions for various systems [24–27] and has also been predicted by calculations [28]. Neagu *et al* studied the surfaces of a $La_{0.52}Sr_{0.28}Ni_{0.06}Ti_{0.94}O_3$ sample by x-ray photoelectron spectroscopy (XPS), as shown in figure 7.10 [2]. Instead of the expected $A_{0.8}BO_3$ stoichiometry, the native surface displayed considerable A-site
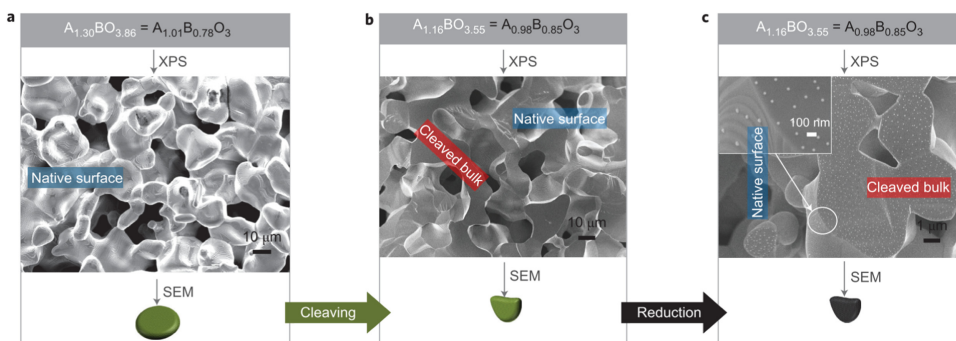
Figure 7.10. Microstructure (obtained via scanning electron microscopy (SEM)) and the corresponding surface stoichiometry (obtained via XPS) of a $La_{0.52}Sr_{0.28}Ni_{0.06}Ti_{0.94}O_3$ porous sample: as prepared (~1400 °C, air), that is, the native surface (a); after cleaving, which exposes the bulk-type surfaces with nominal stoichiometry (b); after reducing the cleaved sample in the XPS in 5%H_2/Ar (30 min isothermal steps at 600 °C, 700 °C, 800 °C, and 900 °C) (c) [2]. Reproduced with permission from [2]. © University of St. Andrews and Dr Dragos Neagu.

and O-site excess, $A_{1.30}B$O$_{3.86}$ (figure 7.10(a)). Szot and co-workers showed that the A-site- and O-site-rich surface layer is usually, as the stoichiometry implies, an A-site- and O-site-excess perovskite variant inherently formed during annealing in oxidizing conditions at high temperatures [29, 30]. Therefore, in A-site deficient perovskites, the native surface layer acts to locally suppress B-site exsolution, as it belongs to the excess perovskite non-stoichiometric class, which does not naturally promote B-site exsolution. Due to the unfavorable conditions for exsolution, the resulting nanoparticle precipitates tend to be very large in dimensions and low in population.

In comparison to native surfaces, cleaved surfaces (i.e. fractured surfaces) display the nominal stoichiometry of the material. During cleaving, most of the fracture occurs through the grains and thus exposes several 'bulk surfaces' of nominal $A_{0.8}B$O$_3$. As shown in figure 7.10(b), where the averaged compositions of the cleaved and native surfaces are measured, the surface A-site excess decreases from $A_{1.3}B$O$_{3.86}$ to $A_{1.16}B$O$_{3.55}$. The importance of studying a cleaved surface is that it represents the exsolution conditions as they were designed. When reduced under the same conditions, the cleaved surfaces are far superior in terms of producing smaller and more uniformly distributed nanoparticles than the native surfaces. As presented in figure 7.10(c), the nanoparticles exsolved on the cleaved surfaces are more abundant and much better distributed than those of the native surfaces. Thus, by investigating cleaved surfaces, one may obtain a more representative perspective of the capability of different non-stoichiometries to produce exsolution [17].

In addition to native and cleaved surfaces, exsolution from a material's surface (which is typically polycrystalline) can differ drastically from area to area of the same material. Such a phenomenon is not rare in exsolution studies, as surfaces separated by grain boundaries also have varying crystallographic orientations. Since the nanoparticles grow epitaxially, surface orientation plays an essential role in determining the crystal structure and the exsolution behavior of the nanoparticles. It has been reported that the exsolved nanoparticle size and population vary dramatically between the (111), (110), and (100) surface orientations, as shown in figure 7.11 [31]. Such a phenomenon could be linked to the differences in interfacial energies as a function of surface orientation; it can be used to control the morphology and nucleation behavior of exsolved nanoparticles. It should also be pointed out that in thin-film exsolution studies, the orientation might be controlled by the strain between the film and the support, thus impacting the exsolution process. Nevertheless, the electrode materials used in SOCs are generally random in orientation, and it is common for the surface orientations to deviate (or tilt) far from the major lattice planes (e.g. (111), (100), (200), etc). Therefore, it is very challenging to use the surface orientations to control nanoparticle exsolution in many practical applications.

Moreover, although less reported, the exsolution behavior of particulate materials varies significantly with their grain size. The grain size reflects the surface area of a particle and correlates closely with the particle's surface energy. In many catalytic applications, e.g. SOC electrodes, catalysts are utilized in particle form, and smaller particles are generally favored since they possess a larger specific surface area, hence
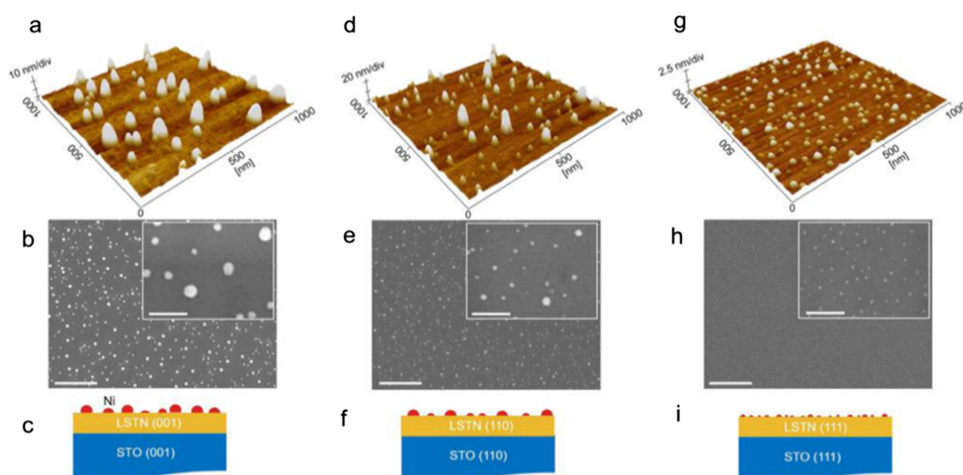
Figure 7.11. Exsolution from $SrTiO_3$ (STO)-supported $La_{0.2}Sr_{0.7}Ti_{0.9}Ni_{0.1}O_{3-\delta}$ films with surface orientations of (a), (b), (c) (001); (d), (e), (f) (110); and (g), (h), (i) (111). Reprinted with permission from [31]. Copyright (2019) American Chemical Society.

better activity. However, in exsolution systems, a 'critical surface area' or 'critical grain size' may exist. As the name suggests, the critical surface area refers to the surface area below which exsolution becomes very difficult or no longer occurs. For example, when the SOC electrode particle size is reduced to ~1 μm, the number of exsolved NPs is very low compared to the number exsolved by electrode particles of ~4 μm. Therefore, the adjustment of particle size could be an effective way of tailoring exsolution. However, there might be trade-offs in terms of SOC performance.

Apart from a material's intrinsic surfaces as discussed above, surfaces that are externally processed or treated can show notably different exsolution properties to those of intrinsic surfaces (either improved or worsened). For example, in some scenarios, the as-prepared material needs to be polished to obtain a large flat area with the desired surface roughness. During polishing, the *A*-site- and O-site-rich surfaces are removed, thus exposing the bulk surfaces. The polished surface is able to generate tremendous amounts of nanoparticles over a large area and can therefore be conveniently used to study the influence of stoichiometry and doping on exsolution. However, it should also be noted that polished surfaces cannot fully represent the intrinsic properties of the materials studied. During polishing, the material's surfaces are highly strained, which may cause the accumulation of certain lattice defects, making the surface energy high. Such modifications would promote the exsolution process in a similar way to the lattice tensile strain effect reported by researchers [17].

In a word, since the surface characteristics affect the exsolution behavior dramatically, it is of paramount importance to understand and study the interrelations between the surface features and the exsolution process. Of all the kinds of surface discussed above, the fractured/cleaved and polished ones should be the best

options for studying the aptitude of different non-stoichiometries to produce exsolution, since they represent identical or nearly identical stoichiometries to that of the material as it was designed. Moreover, using the surface orientation to tune exsolution may be most suitable for thin-film applications, as the catalysts are likely polycrystalline in most catalytic scenarios, thus posing a significant challenge to the qualitative control of their surface lattice structures. In contrast, adjusting the particle size of a catalyst might be the most practical way to tune the exsolution and nanoparticles' traits, especially for SOC applications.

7.3.2.3 Oxygen partial pressure

The exsolution of metal nanoparticles mainly occurs in a reducing atmosphere, i.e. at a low oxygen partial pressure ($p_{O_2} < 10^{-16}$ atm, depending on the system). Therefore, p_{O_2} is probably one of the most important extrinsic factors that critically governs the exsolution process. It has also been widely used to promote and tune the scale of exsolved nanoparticles. The biggest advantage of utilizing p_{O_2} is that it can be conveniently changed to obtain a wide spectrum of either reducing or oxidizing atmospheres, thus providing a handy way to study and control exsolution. For example, p_{O_2} can be changed by mixing H_2 and an inert gas (e.g. N_2, Ar) at varying ratios or by changing the atmospheric temperature or humidity of the gas, etc.

A sufficiently reductive atmosphere creates a gradient of p_{O_2} from the bulk to the surface of the studied material. Such a gradient of p_{O_2} acts as a driving force that induces cation diffusion and subsequent exsolution, and this process starts by stripping away the oxygen atoms from the very top surface layers of the material. The reducible B-site metal cation is then reduced to keep the system charge neutral. Exsolution continues to occur as long as there is a sufficiently high p_{O_2} gradient, and the above process naturally slows down over time due to the limited cation supply.

By carefully adjusting the p_{O_2} of the atmosphere, the composition and properties of exsolved nanoparticles can be tuned. For example, using A-site deficient $Sr_{0.95}Ti_{0.3}Fe_{0.63}Ni_{0.07}O_{3-\delta}$, Barnett et al decreased the p_{O_2} of the atmosphere from 4.0×10^{-20} to 2.6×10^{-20} atm by switching the gas composition from 10% H_2/3% H_2O/87% Ar to 30% H_2/3% H_2O/67% Ar at 850 °C, and observed that the composition of exsolved alloy nanoparticles was altered from $Fe_{0.3}Ni_{0.7}$ to $Fe_{0.5}Ni_{0.5}$. It was predicted that the Fe content should decrease as the p_{O_2} increases [32]. In addition, Yue et al successfully induced the co-exsolution of CeO_2 and Ni nanoparticles by treating $La_{0.8}Ce_{0.1}Ti_{0.6}Ni_{0.4}O_3$ material in air (oxidative, ~1100 °C–1300 °C) and then in 5% H_2/95% Ar (reductive, 900 °C) [33]. This suggests an intriguing use of vastly different p_{O_2} environments to trigger the consecutive exsolution of two functional phases. Moreover, by repetitively switching between reducing/oxidative atmospheres, i.e. applying redox cycling, exsolution could be significantly enhanced. For example, after a $Sr_2Fe_{1.4}Ru_{0.1}Mo_{0.5}O_{6-\delta}$ perovskite was exposed to four sequential redox cycles, the population of exsolved RuFe alloy nanoparticles reached ~21 000 particles μm^{-2}, which was ~3.6 times higher than that of a sample after the first round of reduction treatment [34].

7.3.2.4 Potential bias

The exsolution of finely distributed nanoparticles generally requires a lengthy reduction process (e.g. ~20 h) in either a pure or diluted H_2 atmosphere. The sluggish cation diffusion and exsolution kinetics make the entire process time-consuming, thus chemically induced exsolution is impractical or expensive in many applications. In 2016, a striking electrochemically induced exsolution phenomenon was reported by Irvine's group [18]. In contrast to lengthy chemical reduction, electrochemical reduction allows the exsolution of fine nanoparticles to take place within a couple of minutes. This technique is particularly useful in SOC applications, as the potential bias (i.e. the high electrolysis voltage) can conveniently be applied to the fuel electrode, 'instantly' boosting the performance of the cell due to accelerated exsolution. At 900 °C, the population of the Ni nanoparticles from $La_{0.43}Ca_{0.37}Ni_{0.06}Ti_{0.94}O_{3-\delta}$ induced by potential bias (2 V, 150 s) is significantly higher than that obtained via chemical reduction (5% H_2, 20 h), i.e. 370 versus 90 particles μm^{-2}. The details of the cell performance improvement are discussed in section 7.4.

The slow kinetics of H_2-induced exsolution is probably related to the much lower p_{O_2} experienced by the sample (typically ~10^{-19} atm), compared with the p_{O_2} obtained through an electrolysis voltage (~10^{-35} atm at 2 V). When the voltage is applied, the sudden flux of electrons flowing through the perovskite lattice greatly facilitates particle nucleation, leading to the formation of smaller yet significantly more nanoparticles.

Since the report of electrochemical reduction and its beneficial effects, its application in exsolution systems has been gaining increasing attention. Myung et al employed an electrochemical reduction at 2.3 V to induce the exsolution of Cu nanoparticles from a $La_{0.43}Sr_{0.37}Cu_{0.12}Ti_{0.88}O_{3-\delta}$ (LSCuT) titanate fuel electrode [35]. Compared to its Cu-infiltrated $La_{0.4}Sr_{0.4}TiO_{3-\delta}$ (LST) counterpart, the electrically exsolved Cu–LSCuT displayed much better thermal stability and finer nanoparticle distribution. A cell that used exsolved LSCuT as its fuel electrode exhibited an excellent maximum power density (MPD) of 1.38 W cm^{-2} at 900 °C in 3% H_2O/97% H_2, and superior operational stability was demonstrated at 1.5 A cm^{-2} for ~150 h. Similarly, Fan et al utilized an electrochemical treatment to trigger Co–Fe alloy nanoparticle exsolution from $La_{0.43}Ca_{0.37}Ti_{0.8}Co_{0.1}Fe_{0.1}O_{3-\delta}$ (LCTCF) and demonstrated that the electrocatalytic activity of LCTCF could be manipulated by adjusting the externally applied voltage [36]. The electrically boosted LCTCF cell produced a much higher MPD (896 mW cm^{-2} in 3% H_2O/97% H_2, 3 V for several minutes) than that of its chemically reduced counterpart (210 mW cm^{-2} in 3% H_2O/97% H_2, 20 h) at 900 °C.

Using potential bias to trigger exsolution is effective and particularly useful in SOC applications, as it enables the convenient in situ tuning of the electrode's microstructure and activity to be completed rapidly. Nevertheless, it is worth mentioning that potential bias is not a universal technique and that excessive electrical reduction may lead to material decomposition and thus performance degradation. The underlying mechanism responsible for the characteristics of electrochemical reduction needs further investigation.

In summary, the exsolution phenomenon is fascinating, as it can be optimized through sophisticated material design and post-treatment. In addition to the

controlling factors discussed above (i.e. stoichiometry, surface characteristics, oxygen partial pressure and potential bias), other factors, e.g. light, strain, phase transition, etc. have also been reported to influence the exsolution process to some extent [17, 37, 38]; since these factors are not common practice and are relatively less studied in the SOC field, their discussion is not included in this chapter.

7.4 Examples of the use of exsolution in solid oxide cells

Exsolution-derived nanostructures have been utilized for a wide range of applications, especially in SOCs. Compared to other applications, the use of exsolution materials as electrodes (mainly fuel electrodes) in SOCs offers a couple of unique advantages. First, the fuel atmosphere (e.g. pure or diluted H_2) and high operational temperature (600 °C–900 °C) of SOCs provide ideal conditions for the convenient reduction of the fuel electrode material, triggering the *in situ* exsolution of nanoparticles. Second, the exsolved transition metals (e.g. Ni) are frequently used as anode components in SOFC and exhibit high catalytic activity for fuel oxidation. Third, the exsolved nanocatalysts show superior resistance to agglomeration and coking due to their inherent socketed interface structure. This is particularly useful for the fuel electrodes of SOCs, as these cells often need to be operated with hydrocarbon fuels in the long term. Last but not least, as SOCs are electrochemical devices, a large electrical bias can be applied to the electrode materials to trigger abundant nanoparticle exsolution in a short space of time.

Therefore, the study and application of exsolved materials in SOCs has been increasing exponentially in recent years. In addition to the discussion above, this growth has been motivated by the fact that exsolution can be tuned by factors such as stoichiometry, the surface characteristics of the parent material, oxygen partial pressure, etc. enabling delicate control of the material's functionality to address varying application scenarios in SOCs. Specifically, introducing *A*-site deficiency into a perovskite fuel electrode promotes *B*-site cation exsolution and hence improves SOC performance; implementing external potential bias can facilitate the exsolution of large quantities of fine NPs and thus notably enhance the catalytic activity of the material. In this context, this section introduces the ways in which exsolution can yield material functionality and advancement in SOCs, focusing in particular on work published since 2013. The progressive development and optimization of exsolution systems in order to improve SOC performance is summarized and discussed. The following sections are categorized on the basis of the exsolved species, with a focus on the performance improvement resulting from exsolution.

7.4.1 Metal and metal alloy exsolution

To date, Ni has undoubtedly been the most investigated transition metal for exsolution, due to the ease with which it exsolves and its superior catalytic activity as a fuel electrode for SOCs. The extensive application of exsolved Ni systems has been advocated, as it delivers higher activity and durability than the conventional deposition process. Evidence suggests that the exsolution of large quantities of Ni

nanoparticles facilitates the catalysis of reactant molecules, e.g. H_2 absorption and dissociation, thus improving Ni's catalytic activity. In SOFCs, the H_2 fuel dissociative adsorption that takes place on exsolved Ni is followed by the adsorbed atomic hydrogen spilling over onto the electrode oxide surface for electrochemical oxidation. Tsekouras *et al* examined the performance of Ni-exsolved $La_{0.4}Sr_{0.4}Ni_{0.06}Ti_{0.94}O_{3-\delta}$ as a cathode for solid oxide electrolyzer cell (SOEC) steam electrolysis [39]. The presence of electrocatalytically active Ni nanoparticles and higher oxygen vacancy ($V_O^{\cdot\cdot}$, introduced by exsolution) concentrations drastically lowered the activation barrier of steam electrolysis as compared to the undoped counterpart, i.e. $La_{0.4}Sr_{0.4}TiO_{3-\delta}$ (LST). Therefore, compared to an LST cell, the use of Ni exsolution led to a step change in steam electrolysis performance, in which the current density (j) increased from 0.09 A cm^{-2} to 0.19 A cm^{-2} at 1.6 V and at 900 °C in 47% H_2O/53% N_2. Sun *et al* prepared Ni-doped $(La_{0.7}Sr_{0.3})(Cr_{0.85}Ni_{0.15})O_{3-x}$ (LSCNi) for SOFC anodes, and the exsolution of abundant Ni nanoparticles remarkably increased the conductivity and catalytic activity of this material [19]. The MPD of the exsolved cell was 460 mW cm^{-2} in 5000 ppm of H_2S–H_2, compared to only 135 mW cm^{-2} for cells with stoichiometric LSCNi, which had little Ni exsolution. The performance of these exsolved materials is still poor compared to the performance of state-of-the-art Ni–YSZ, mainly due to the low activity of the fuel electrode materials themselves as well as the thick electrolyte support. Continuing efforts have been devoted to material design and cell structure optimization in order to improve SOC performance.

Later, in 2016, an innovative and exciting method for triggering exsolution was reported by Irvine *et al* [18]. In contrast to the lengthy chemical reduction (by H_2, generally taking 10–30 h), Ni nanoparticle exsolution from a $La_{0.43}Ca_{0.37}Ni_{0.06}Ti_{0.94}O_{3-\gamma}$ (LCNT) fuel electrode was achieved at 2 V in 50% H_2O/N_2 for a few seconds (see section 7.3 for a detailed mechanistic discussion). Moreover, as compared to H_2 reduction, the electrochemical reduction led to a higher degree of exsolution, a higher particle population (370 versus 90 particles μm^{-2}), and a smaller average particle size (15 versus 20 nm). The electrochemical process not only promotes Ni exsolution, but also effectively enhances the electronic and ionic conductivities of the titanate electrode. Therefore, the performance of an LCNT (~10 μm)|$Zr_{0.89}Sc_{0.1}Ce_{0.01}O_{2-\gamma}$ (~80 μm)|$Zr_{0.89}Sc_{0.1}Ce_{0.01}O_{2-\gamma}$–$(La_{0.8}Sr_{0.2})_{0.95}MnO_{3-\gamma}$ (~20 μm) cell was 'switched on' drastically. The MPD of the cell in SOFC mode reached ~2 W cm^{-2} at 900 °C in 3% H_2O/H_2, while the current density in SOEC mode soared to 2.75 A cm^{-2} at 1.3 V and 900 °C in 50% H_2O/N_2.

In addition to the predominant Ni exsolution studies, other transition metals such as Fe, Co, Cu, and their alloys are actively being investigated for SOC applications. As discussed in section 7.3, the exsolution of Fe is more difficult than that of Ni. Tsekouras *et al* revealed that the performance of Fe-exsolved $La_{0.4}Sr_{0.4}Fe_{0.06}Ti_{0.94}O_{3-\delta}$ (LSFT) is much lower than that of its Ni doped and exsolved counterpart when used as a SOEC steam electrolysis cathode, with significantly lower nanoparticle coverage [39]. However, Fe alloyed with other exsolved metals is very effective in promoting the catalytic activity of these materials. Sun *et al* studied the effect of Fe doping on the electrocatalytic activity of a $(La_{0.7}Sr_{0.3})(Cr_{0.85}Ni_{0.15-x}Fe_x)O_{3-\delta}$ (LSCNi–Fe,

$x = 0.0375$)–YSZ composite fuel electrode. The exsolved bimetallic Ni–Fe nanoparticles promoted the SOFC performance in 5000 ppm of H_2S–H_2 fuel, exhibiting a MPD of ~600 mW cm^{-2} at 800 °C (compared to ~500 mW cm^{-2} for LSCNi, $x = 0$). It has been suggested that the Fe doping not only altered the material's reduction behavior but also increased the number of oxygen vacancies [20]. Ni–Fe alloy exsolution has also been instrumental in improving SOEC performance. Liu *et al* investigated the activity of an Fe–Ni exsolved $La_{0.6}Sr_{0.4}Fe_{0.8}Ni_{0.2}O_{3-\delta}$ (LSFN)–GDC composite cathode for CO_2 electrolysis [40]. The results indicated that Fe–Ni exsolution significantly improved the cathode kinetics for CO_2 electrolysis, with a high j of 1.78 A cm^{-2} and a high faradaic efficiency (98.8%) at 1.6 V and 850 °C. The exsolved cathode material also displayed superior tolerance to carbon deposition. Doping a small amount of Fe into a Ni-containing material enhances its activity; similarly, adding a small quantity of Ni to a ferrite enhances its performance. Barnett *et al* [32] evaluated the effectiveness of doping Ni into a ferrite, $Sr_{0.95}(Ti_{0.3}Fe_{0.7-x}Ni_x)O_{3-\delta}$ (STFN, $x = 0.07$), and discovered exsolved $Ni_{0.5}Fe_{0.5}$ nanoparticles uniformly dispersed on the perovskite surface, whereas no nanoparticles were seen on $SrTi_{0.3}Fe_{0.7}O_{3-\delta}$ (STF), as seen in figure 7.12(a). The addition of Ni to STFN, i.e. the exsolution of $Ni_{0.5}Fe_{0.5}$ particles, dramatically reduced the anode polarization by as much as four times at 800 °C in 3% H_2O/H_2, resulting in an MPD of ~1 W cm^{-2} (see figure 7.12(b)).

Compared to Ni exsolution systems, Co metal can also readily exsolve due to its similar Gibbs free energy of reduction (see section 7.3.1 for details). The application of Co exsolution systems in SOCs has also been widely reported. An interesting work published by Sun *et al* found that the crystal structure of a Co-doped perovskite, $Pr_{0.5}Ba_{0.5}Co_{0.1}Mn_{0.9}O_x$ (PBCM), was altered to a layered structure, $PrBaMn_{1.8}Co_{0.2}O_5$, by reduction, which triggered the exsolution of massive quantities of finely dispersed Co nanoparticles [38]. Density functional theory (DFT)
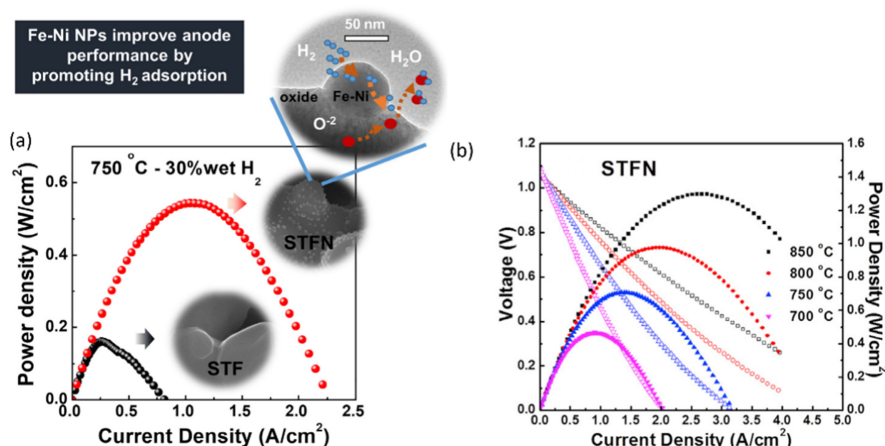

Figure 7.12. (a) A comparison of the SOFC performances of reduced STF and STFN anode cells at 750 °C in 30% H_2/67% Ar/3% H_2O and (b) the *I–V* curves and power output of the STFN cell at different temperatures in 3% H_2O/H_2. Reprinted from [32], Copyright (2018), with permission from Elsevier.
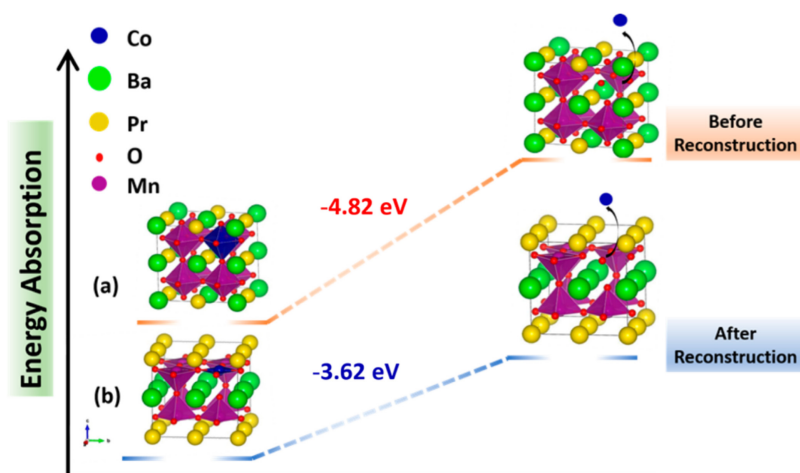
Figure 7.13. A schematic diagram of PBCM (a) before and (b) after crystal reconstruction, showing the ordering of each element, the formation of oxygen vacancies, and the exsolved Co. Reproduced with permission from [38]. Copyright (2016) American Chemical Society.

calculations suggested that the crystal reconstruction (CR, i.e. phase change or lattice rearrangement) of the PBCM double perovskite induced the creation of large numbers of ordered oxygen vacancies and thus the loss of coordinated oxygen surrounding Co cations, which served as the driving force for fast Co nanoparticle growth. Figure 7.13 shows a schematic diagram of the simulated PBCM exsolution process before and after reconstruction, which indicates the relatively kinetically unfavorable exsolution of Co from perovskite without CR (the Co formation energy is -4.82 eV without CR vs -3.62 eV with CR) due to its full coordination properties and the absence of consecutive diffusion paths. At 900 °C, a fuel cell using an exsolved PBCM–GDC composite anode showed a good MPD of 900 mW cm^{-2} with syngas; it also displayed superior CO_2 electrolysis performance with a high j of 2.5 A cm^{-2} at 1.5 V in 70 vol% CO_2/30 vol% CO.

In addition to the exsolution of Co alone, alloys of Co with other metals such as Fe have also been investigated by many research groups. In a direct hydrocarbon-fed SOFC study, exsolved Co–Fe nanoparticles were reported to boost the conductivity, stability, and activity of the perovskite $Pr_{0.4}Sr_{0.6}Co_{0.2}Fe_{0.7}Nb_{0.1}O_{3-\delta}$ (PSCFN) [41]. An exsolved Co–Fe–PSCFN anode cell displayed a decent power output with wet C_3H_8 (3% H_2O) fuel, achieving an MPD of 0.92 W cm^{-2} at 850 °C; the single cell was able to run stably in wet C_3H_8 at a j of 0.4 A cm^{-2} at 800 °C for ~600 h. Moreover, some studies found that exsolved Co–Fe alloy particles were capable of redissolving into and regenerating from the substrate lattice under certain conditions. Lai *et al* presented a perovskite SOFC anode material $La_{0.3}Sr_{0.7}Cr_{0.3}Fe_{0.6}Co_{0.1}O_{3-\delta}$ (LSCrFeCo), which allowed the exsolution (upon reduction) and dissolution (upon oxidation) of Co–Fe alloy nanoparticles to take place at 700 °C. The Co–Fe nanocatalysts improved the MPD of an LSCrFeCo–GDC composite anode by more than 75% in comparison to that of its cobalt-free
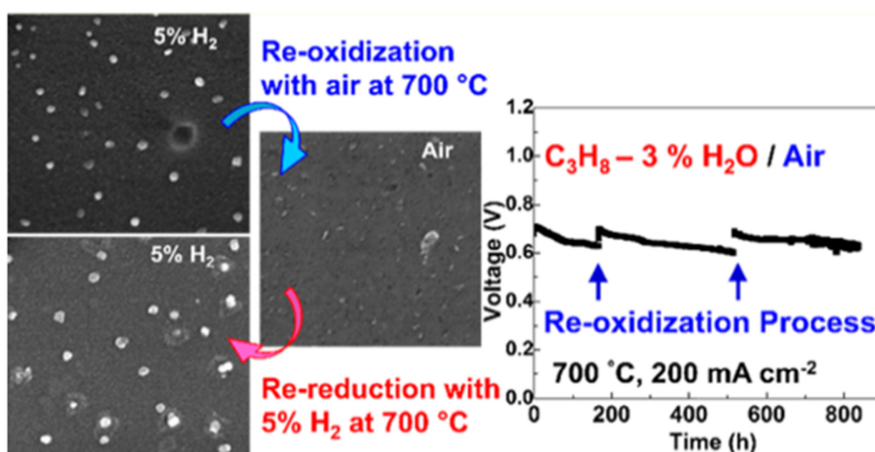
Figure 7.14. A self-regenerating LSCrFeCo anode drives off carbon deposition in C_3H_8 fuel and reactivates its catalyst during redox cycles. Reprinted with permission from [42]. Copyright (2018) American Chemical Society.

counterpart; the self-regenerating anode (i.e. dissolving and regenerating Co–Fe nanoparticles) was able drive off carbon deposition in propane fuel and reactivate its catalyst during redox cycles [42], as presented in figure 7.14.

The exsolution of alloy nanoparticles can also be achieved by combining infiltration and *in situ* exsolution techniques. An interesting study published by Kim *et al* reported the use of a smart selective exsolution process to produce alloyed Co–Fe nanoparticles through topotactic ion exchange (see figure 7.15(b)), in which infiltrated Fe guest cations were exchanged with Co host cations in $PrBaMn_{1.7}Co_{0.3}O_{5+\delta}$ (PBMCo) [15]. This process changed the host composition to $PrBaMn_{1.7}Fe_{0.3}O_{5+\delta}$ (PBMF), liberating all the Co cations from the host lattice, thus leading to an increase in the number of exsolved nanoparticles. According to the DFT calculation in figure 7.15(a), the topotactic cation exchange between Co and Fe occurred spontaneously due to the favorable incorporation energy (-0.41 eV) and exchange energy (-0.34 eV) of the infiltrated guest Fe on the host material PBMCo. The MPD of the PBMCo–Fe cell reached 1.83 W cm^{-2} in humidified H_2 (3% H_2O) at 800 °C, as displayed in figure 7.15(c).

In comparison to the Ni, Co, and Fe exsolution systems, the study of Cu exsolution has been relatively less reported, partly due to the difficulty in doping an adequate amount of Cu into the perovskite lattice and its subsequent exsolution. Cu is a good catalyst for SOC fuel electrodes, and it also improves their resistance to coking and sulfur poisoning. Ma *et al* managed to dope 15 mol.% Cu into the *B*-site of $La_{0.5}Sr_{0.5}Fe_{0.8}Cu_{0.15}Nb_{0.05}O_{3-\delta}$ (LSFCNb), and the exsolution of Cu was realized after reduction at 800 °C [43]. A symmetrical cell that used LSFCNb as the fuel and air electrodes showed good performance in H_2, syngas, and H_2S-containing H_2 fuels, with MPDs of 0.76, 0.64, and 0.71 W cm^{-2} at 800 °C, respectively. However, the LSFCNb oxide decomposed after reduction, forming a composite consisting of a K_2NiF_4-type $SrFeLaO_4$ layered perovskite, $LaFeO_3$, and Cu. It appears that the
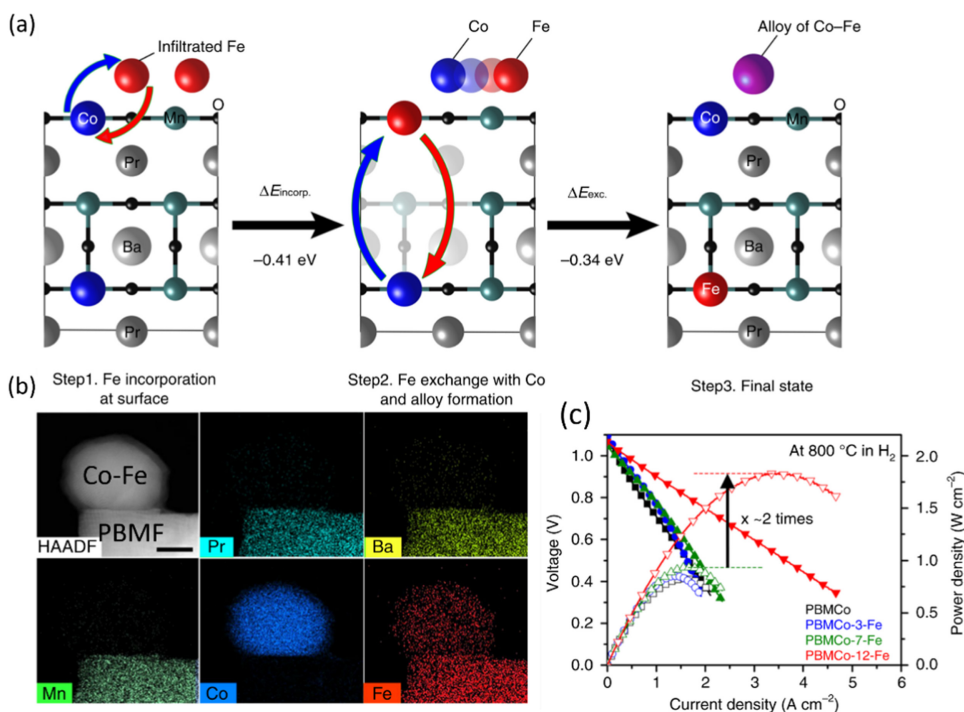
Figure 7.15. (a) Topotactic ion exchange energetics for the mechanism of particle exsolution via Fe infiltration on a PBMCo surface. (b) Scanning transmission electron microscopy–energy dispersive x-ray spectroscopy (STEM-EDS) element map of Pr, Ba, Mn, Co, and Fe; scale bar 20 nm. (c) $I–V$ curves and the MPDs of PBMCo–x-Fe samples at 800 °C in humidified H_2 (3% H_2O); x stands for the amount (wt.%) of Fe infiltrated. Reproduced with permission from reference [15] Copyright © 2019, The Author(s). With permission of Springer.

parent perovskite was not robust enough to retain its structure upon reduction and Cu exsolution. A similar phenomenon was also mentioned in a report in which Ni-doped spinel oxide $CuFe_2O_4$ decomposed after reduction, forming Cu–Fe–Ni alloy nanoparticles [44]. A recent Cu exsolution study was reported by Myung *et al* [35]. In their study, 12 mol.% Cu was successfully doped into $La_{0.43}Sr_{0.37}Cu_{0.12}Ti_{0.88}O_{3-\delta}$ (LSCuT) via a solid-state synthesis method. The exsolution of Cu was achieved by electrochemical reduction (~a few seconds) at 2.3 V and at 900 °C, as shown in figures 7.16(a) and (b). The exsolved LSCuT cell exhibited an MPD of 1.38 W cm^{-2} at 900 °C in wet H_2 and excellent operational stability for ~150 h (in figures 7.16(c) and (d)). The exsolution of Cu nanoparticles did not decompose the perovskite structure of the LSCuT titanate.

In brief, metal exsolution imparts unique, additional, and enhanced properties to the support material, and depending on the metal species, the functionality of the material can be tuned precisely. Apart from the transition metals discussed above, many other metal exsolution systems are employed for SOC applications, e.g. noble metals (Ag, Ir, Ru, Pd, etc.) and ternary alloy exsolution systems, which further broadens the applicability of exsolution materials to SOCs. For detailed
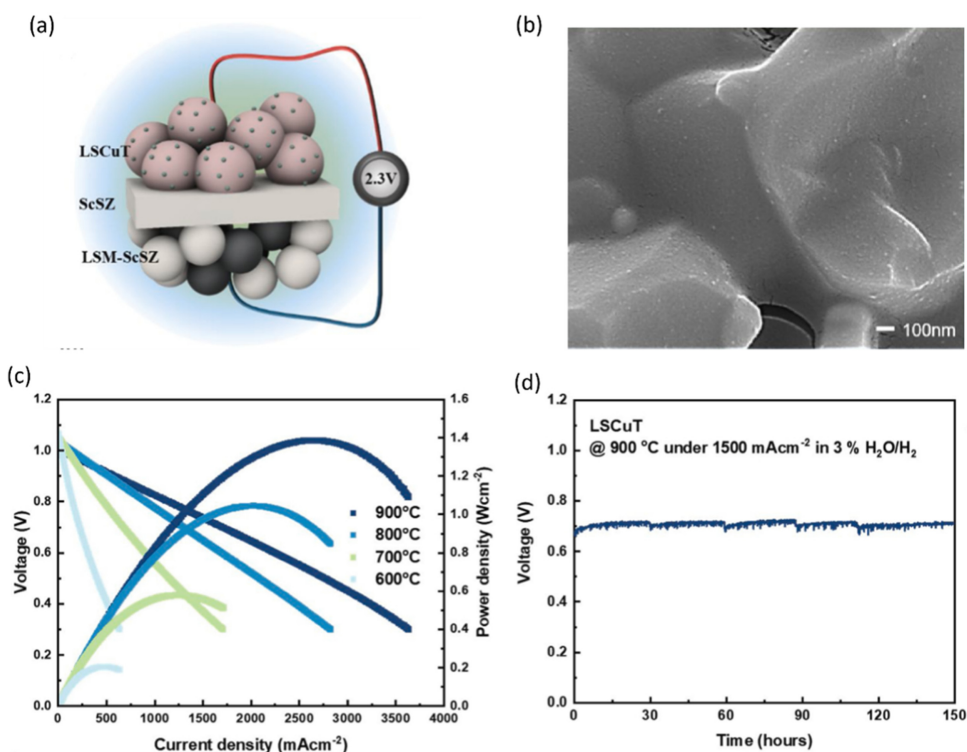
Figure 7.16. (a) A schematic of the electrochemical reduction of the LSCuT cell at 2.3 V. (b) An SEM image of the electrochemically reduced LSCuT electrode. (c) *I–V* curves and power density of the reduced LSCuT cell at different temperatures and (d) the results of a test of its stability at 900 °C in 3% H_2O/H_2. Reprinted from [35], Copyright (2020), with permission from Elsevier.

information, the reader is referred to two recent review papers published by Kousi *et al* [45] and Tang *et al* [46].

7.4.2 Metal and metal oxide exsolution

In addition to *B*-site transition-metal exsolution, oxide segregation/exsolution from the perovskite support may also occur along with the *B*-site metal exsolution. The co-exsolved oxides can have many forms and compositions, depending on the structure of the parent perovskite structure. As the segregated oxide can also influence the properties of the base material, it is equally important to discuss and explore the potential of oxide co-exsolution in energy applications.

Kim *et al* studied an *A*-site layered oxygen-deficient perovskite, $NdBaMn_2O_{5+\delta}$ (NBMO), and discovered that the exsolution of MnO occurred during a reduction process [47]. The perovskite experienced a phase transition, forming an *A*-site layered perovskite structure, as shown in figure 7.17. As an anode, the MnO-nanoparticle-decorated NBMO exhibited excellent SOFC performance, showing a MPD of ~0.6 W cm^{-2} at 800 °C in wet H_2. However, the stability of this exsolved MnO anode under SOFC operating conditions was not studied; thus it is unclear whether
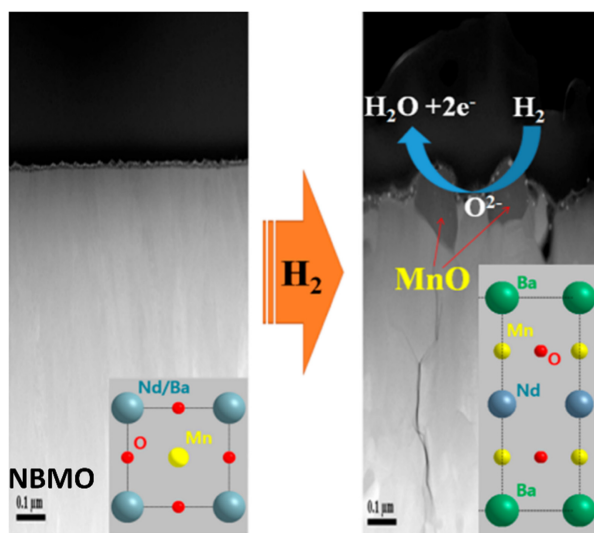
Figure 7.17. High-angle annular dark-field scanning TEM image of $Nd_{0.5}Ba_{0.5}MnO_3$ film (a) before and (b) after reduction. The precipitation of MnO after reduction is highlighted. Reprinted with permission from [47]. Copyright (2017) American Chemical Society.

this material can run stably over a long time period. Guo *et al* [48] reported an *A*-site and *B*-site co-exsolution phenomenon that occurred in a ferrite perovskite, $Ba_{0.3}Sr_{0.7}Fe_{0.9}Mn_{0.1}O_{3-\delta}$ (BSFM), in which Fe nanoparticles and SrO/BaO whiskers were exsolved after reduction at 800 °C for 5 h in 50% H_2/50%Ar gas. While the perovskite structure was retained, the exact mechanism of co-exsolution was not discussed and thus remains unclear. The exsolved BSFM anode exhibited an MPD of 538 mW cm^{-2} at 800 °C in H_2, and decent stability was demonstrated for 60 h. The exsolved SrO/BaO whiskers in the anode were speculated to function synergistically with Fe nanoparticles in improving the oxygen dissociation/dissolution kinetics.

Moreover, the co-exsolution of well-known active oxides such as CeO_2 along with transition metals can be an effective way to reinforce the functionality of the base material. Li *et al* doped 5 at.% Ru into the perovskite $Sr_{0.8}Ce_{0.2}FeO_3$ (SCF), and the Ru-doped SCF was used as the electrodes of a symmetrical SOFC (SSOFC) [49]. Surface segregation of nanoscale SrO, CeO_2, and Ru^0 was observed under fuel conditions. The symmetrical cell showed MPDs of 846 mW cm^{-2} and 310 mW cm^{-2} at 800 °C in H_2 and C_3H_8, respectively. It was suggested that the exsolution of Ru^0 facilitated the H_2 oxidation reaction and that the CeO_2 reinforced the absorption of propane molecules, while the simultaneous superficial exsolution of SrO was found to be important for coke resistance under carbonaceous fuel. Nevertheless, the segregation/exsolution of $SrO–CeO_2–Ru^0$ was due to the surface decomposition of the support, and the distribution of ceria was difficult to identify. In another study, the co-exsolution of clearly visible ceria cubes and Ni nanoparticles was realized from a $La_{0.8}Ce_{0.1}Ni_{0.4}Ti_{0.6}O_3$ (LCeNT) host material [33]. The exsolution of ceria cubes was achieved by annealing LCeNT in air at high temperature (1000–1300 °C),
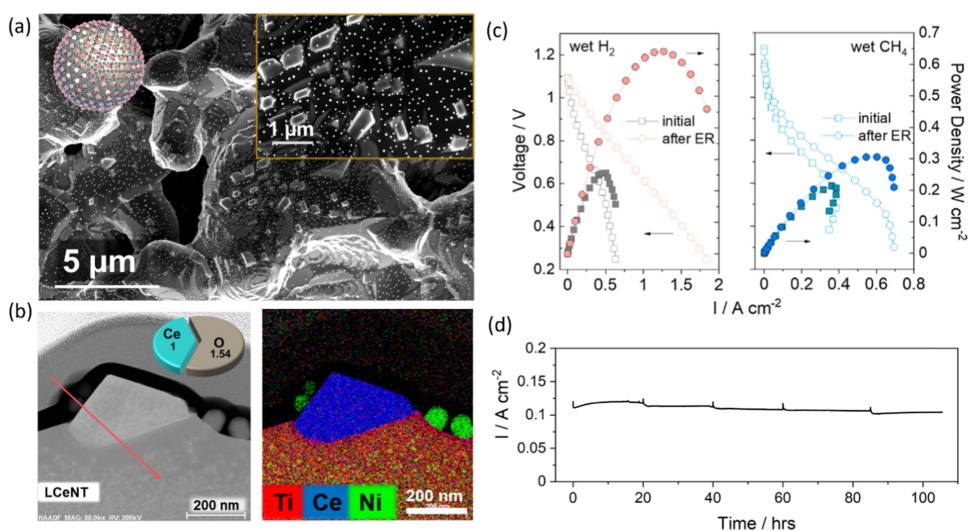
Figure 7.18. (a) An SEM image of the exsolved LCeNT with CeO_2 cubes and Ni nanoparticles. (b) STEM-EDS element map at the exsolved interface, showing the composition of the ceria, the Ni, and the substrate. (c) $I–V$ curves and power densities of the exsolved LCeNT cell at 900 °C fed with wet H_2 and wet CH_4 (3% H_2O). (d) Stability test of the exsolved LCeNT cell in wet CH_4 at 850 °C and at 0.7 V. Reproduced from [33], Copyright (2021), with permission from Elsevier.

while the subsequent Ni exsolution was triggered by a reduction treatment; see figures 7.18(a) and (b). The perovskite structure of LCeNT was preserved throughout the treatment. While the exsolved Ni nanoparticles favor H–H and C–H bond breaking, CeO_2 can improve the material's coke resistance. The co-exsolved LCeNT cell showed good performance in H_2 and CH_4 fuels, with MPDs of 642 and 306 mW cm^{-2} at 900 °C, respectively (in figure 7.18(c)); superior stability was demonstrated by an extended period of operation (~105 h) in 3% H_2O/CH_4 at 850 °C and at 0.7 V, as shown in figure 7.18(d).

In a word, a remarkable improvement in the performance of SOCs due to the use of exsolution has been widely reported in the past decade, and the exsolution technique has been perceived as an effective and versatile way to reinforce the functionality of the electrode material. While keeping the structure of the base material stable is important, it is intriguing that the exsolved species and composition can be adjusted through sophisticated material design and post-treatment.

7.5 Advances and outlook

As a result of vigorous development in materials engineering and the mechanistic study of exsolution, substantial advances have been made with increasingly high performance reported, much higher than that achieved using conventional Ni–YSZ cermet electrodes in SOCs. Some efforts have been made to evaluate the stability of emerging exsolution materials in SOCs, though the duration of the stability tests needs to be significantly extended to validate the superior durability and cost-effectiveness of these materials in SOCs for commercial applications. Continuous efforts have been

made to improve the depth of understanding of the mechanisms controlling the exsolution process and the particle–substrate interface, as well as to extend the concept to a wide range of structures, such as fluorite structures, spinel structures, etc.

Exsolution has predominantly been applied in oxide materials with perovskite-type structures, including single perovskites (ABO_3), double perovskites ($A_2BB'O_{6-\delta}$ and $AA'B_2O_{5+\delta}$), and Ruddlesden–Popper (RP) phases (such as $A_2BO_{4+\delta}$), as already explained in previous sections. In addition, there have been a few reports of the use of exsolution in compounds other then perovskite-derived structures in SOC applications. Kui *et al* explored $NiMn_2O_4$ mixed with Ni or Ni–YSZ, (Ni, Cu)-doped ceria ($CeO_{2-\delta}$), and $Nb_{1.33}(Ti_{0.8}M_{0.2})_{0.67}O_4$ (M = Mn, Cr) as candidate cathode materials for CO_2 electrolysis through exsolution manipulation [50]. In the mixtures of $NiMn_2O_4$–Ni or –Ni/YSZ, the spinel-type $NiMn_2O_4$ decomposed to metallic Ni and MnO_x during reduction, resulting in nanosized MnO_x anchored on a metallic Ni or a Ni–YSZ composite cathode. The resultant MnO_x–Ni interfaces were found to be critical and advantageous for promoting the chemisorption of CO_2 molecules compared to a Ni-only cathode. Similarly, in the case of Ni/Cu-doped ceria and $Nb_{1.33}(TiM)_{0.67}O_4$, favorable oxygen non-stoichiometry was introduced by doping, which was beneficial for CO_2 accommodation on the surface according to DFT calculations. The coupling of an *in situ* exsolved interface and the oxygen vacancies created by doping and reduction greatly facilitated the oxygen transfer processes and improved electrode activity for CO_2 electrolysis. These results prove that exsolution is a very useful and intriguing platform for creating functionally active interfaces in a wide range of structures, which can be exploited to guide the development of materials and material design in SOCs.

In addition to an expansion in the number of structures that accommodate the exsolution concept, we are seeing the emergence of new phenomena discovered in exsolution materials that have been applied in SOCs to enhance electrode activity, such as topotactic exsolution, redox cycling-promoted exsolution, etc (see section 7.4). These new discoveries help to tackle the issues associated with exsolution, namely, that it is generally a slow and time-consuming process and often generates insufficient nanoparticles. The topotactic exsolution reported in the $PrBaMn_{1.7}Co_{0.3}O_{5+\delta}$ system (see the explanation near figure 7.15 in section 7.4) showed that cation exchange due to the distinct segregation energies of metals in the host lattice can be utilized to speed up the production of sufficient nanoparticles for various applications. Although there are only a few examples in double-perovskite materials, this approach can potentially be extended to other perovskite-related structures, using a better understanding of the fundamentals controlling metal diffusion kinetics and their stability in the host structure. The topotactic exsolution concept, in which the guest ions (introduced by a deposition technique, e.g. impregnation) are exchanged with host ions, also demonstrates a possible synergy between the exsolution and deposition techniques that can be used to generate advanced nanomaterials; however, this perspective needs to be validated by further development.

It is important to point out that the fast development of *in situ* characterization techniques, especially those that can work at high temperatures (600 °C–900 °C), has contributed significantly to the advances made in exsolution materials; such techniques have been shown to be extremely helpful tools for elucidating the intricate

processes and reaction mechanisms involved in exsolution and its applications. Real-time recording of individual nanoparticle growth at the surface of perovskite oxides became possible using next-generation environmental TEM with ultrahigh spatial and temporal resolutions [51]. An analysis of this data disclosed the atomic-scale processes that underpin the formation of socketed, highly strained interfaces that give exsolved nanoparticles their outstanding stability and reactivity. Using operando photoelectron spectroscopy at SOEC operating temperatures, Opitz and co-workers revealed the formation of a carbonate intermediate that developed on the oxide surface upon cathodic polarization; its amount increased with the concentration of oxygen vacancies in the thin-film electrode material, which suggested that vacant oxygen lattice sites were the predominant adsorption sites for CO_2, in agreement with the proposals of other researchers [34, 50, 52]. It is not our intention to give an exhaustive list, but there are many examples of the use of *in situ*/operando techniques to study exsolution materials as well as their applications in SOCs, including steam electrolysis and CO_2 electrolysis, which are instrumental in gaining insights into mechanistic understanding as well as materials design and device operation [53–55]. However, it is worth noting that the further development of these techniques, especially those that can accommodate realistic devices and operating conditions, is critical. Today, many of these *in situ*/operando measurements are performed using a simplified model cell configuration under compromised conditions due to instrumental limitations, which might limit the relevance of the results to real cell operations in SOCs.

In conclusion, exsolution provides a flexible and versatile platform for growing and tuning nanomaterials that are highly desirable for use in SOCs in order to maximize their performance and enhance their stability. Compared to the infiltration technique, exsolution processing offers great control over particle size and population as well as stronger interfacial interactions between particles and their support due to the socketed nature of the nanoparticles, which leads to their outstanding thermal stability, excellent resistance to coking, and tolerance of sulfur poisoning. Exsolution has been subjected to rapid development, and great advances have been made in materials design, property tuning, mechanistic understanding, and the exploration of functionality, taking advantage of the increasing effort being invested in *in situ*/operando characterization techniques and computational modeling development. Emerging new phenomena have been discovered, and there is a vast space for the further development of these materials (e.g. new compositions and/or advanced processing to speed up the generation of sufficient nanoparticles) and for an improved understanding of the structure–property–performance relationship, as well as the continued optimization of material applications in SOCs to provide enhanced performance and prolonged operation at reduced cost, eventually leading to accelerated commercialization.

References

[1] Neagu D, Tsekouras G, Miller D N, Menard H and Irvine J T S 2013 In situ growth of nanoparticles through control of non-stoichiometry *Nat. Chem.* **5** 916–23

[2] Neagu D 2013 Materials and microstructures for high temperature electrochemical devices through control of perovskite defect chemistry *PhD Thesis* (University of St Andrews) https://research-repository.st-andrews.ac.uk/handle/10023/3606

[3] Nishihata Y, Mizuki J, Akao T, Tanaka H, Uenishi M, Kimura M, Okamoto T and Hamada N 2002 Self-regeneration of a Pd-perovskite catalyst for automotive emissions control *Nature* **418** 164–7

[4] Tanaka H, Taniguchi M, Uenishi M, Kajita N, Tan I, Nishihata Y, Mizuki J, Narita K, Kimura M and Kaneko K 2006 Self-regenerating Rh- and Pt-based perovskite catalysts for automotive-emissions control *Angew. Chem. Int. Ed. Engl.* **45** 5998–6002

[5] Madsen B D, Kobsiriphat W, Wang Y, Marks L D and Barnett S A 2007 Nucleation of nanometer-scale electrocatalyst particles in solid oxide fuel cell anodes *J. Power Sources* **166** 64–7

[6] Madsen B D, Kobsiriphat W, Wang Y, Marks L D and Barnett S 2007 SOFC Anode performance enhancement through precipitation of nanoscale catalysts *ECS Trans.* **7** 1339–48

[7] Kobsiriphat W, Madsen B D, Wang Y, Marks L D and Barnett S A 2009 $La_{0.8}Sr_{0.2}Cr_{1-x}Ru_xO_{3-\Delta}$–$Gd_{0.1}Ce_{0.9}O_{1.95}$ solid oxide fuel cell anodes: Ru precipitation and electrochemical performance *Solid State Ion.* **180** 257–64

[8] Bierschenk D M, Potter-Nelson E, Hoel C, Liao Y, Marks L, Poeppelmeier K R and Barnett S A 2011 Pd-substituted $(La,Sr)CrO_{3-\Delta}$–$Ce_{0.9}Gd_{0.1}O_{2-\Delta}$ solid oxide fuel cell anodes exhibiting regenerative behavior *J. Power Sources* **196** 3089–94

[9] Neagu D, Oh T S, Miller D N, Menard H, Bukhari S M, Gamble S R, Gorte R J, Vohs J M and Irvine J T S 2015 Nano-socketed nickel particles with enhanced coking resistance grown *in situ* by redox exsolution *Nat. Commun.* **6** 8120–7

[10] Neagu D *et al* 2017 Demonstration of chemistry at a point through restructuring and catalytic activation at anchored nanoparticles *Nat. Commun.* **8** 1855

[11] Irvine J T S, Neagu D, Verbraeken M C, Chatzichristodoulou C, Graves C and Mogensen M B 2016 Evolution of the electrochemical interface in high-temperature fuel cells and electrolysers *Nat. Energy* **1** 15014–26

[12] Connor P A *et al* 2018 Tailoring SOFC electrode microstructures for Improved performance *Adv. Energy Mater.* **8** 1800120

[13] Papaioannou E I, Neagu D, Ramli W K W, Irvine J T S and Metcalfe I S 2018 Sulfur-tolerant, exsolved Fe–Ni alloy nanoparticles for CO oxidation *Top. Catal.* **62** 1149–56

[14] Park S, Kim Y, Noh Y, Kim T, Han H, Yoon W, Choi J, Yi S-H, Lee W-J and Kim W B 2020 A sulfur-tolerant cathode catalyst fabricated with *in situ* exsolved CoNi alloy nanoparticles anchored on a Ruddlesden–Popper support for CO_2 electrolysis *J. Mater. Chem.* A **8** 138–48

[15] Joo S, Kwon O, Kim K, Kim S, Kim H, Shin J, Jeong H Y, Sengodan S, Han J W and Kim G 2019 Cation-swapped homogeneous nanoparticles in perovskite oxides for high power density *Nat. Commun.* **10** 697

[16] Gao Y, Chen D, Saccoccio M, Lu Z and Ciucci F 2016 From material design to mechanism study: nanoscale Ni exsolution on a highly active *A*-site deficient anode material for solid oxide fuel cells *Nano Energy* **27** 499–508

[17] Han H, Park J, Nam S Y, Kim K J, Choi G M, Parkin S S P, Jang H M and Irvine J T S 2019 Lattice strain-enhanced exsolution of nanoparticles in thin films *Nat. Commun.* **10** 1471

[18] Myung J H, Neagu D, Miller D N and Irvine J T S 2016 Switching on electrocatalytic activity in solid oxide cells *Nature* **537** 528–31

[19] Sun Y, Li J, Zeng Y, Amirkhiz B S, Wang M, Behnamian Y and Luo J 2015 A-site deficient perovskite: the parent for *in situ* exsolution of highly active, regenerable nano-particles as SOFC anodes *J. Mater. Chem.* A **3** 11048–56

[20] Sun Y F, Li J H, Cui L, Hua B, Cui S H, Li J and Luo J L 2015 A-site-deficiency facilitated *in situ* growth of bimetallic Ni–Fe nano-alloys: a novel coking-tolerant fuel cell anode catalyst *Nanoscale* **7** 11173–81

[21] Ding S, Li M, Pang W, Hua B, Duan N, Zhang Y-Q, Zhang S-N, Jin Z and Luo J-L 2020 A-site deficient perovskite with nano-socketed Ni–Fe alloy particles as highly active and durable catalyst for high-temperature CO_2 electrolysis *Electrochim. Acta* **335** 135683

[22] Hu S, Zhang L, Cai L, Cao Z, Jiang Q, Yu W, Wu Y, Zhu X and Yang W 2020 Iron stabilized 1/3 A-site deficient La–Ti–O perovskite cathodes for efficient CO_2 electroreduction *J. Mater. Chem.* A **8** 21053–61

[23] Yu N, Jiang G, Liu T, Chen X, Miao M, Zhang Y and Wang Y 2020 Understanding the A-site non-stoichiometry in perovskites: promotion of exsolution of metallic nanoparticles and the hydrogen oxidation reaction in solid oxide fuel cells *Sustain. Energy Fuels* **5** 401–11

[24] Horvath G, Gerblinger J, Meixner H and Giber J 1996 Segregation driving forces in perovskite titanates *Sens. Actuators* B **32** 93–9

[25] Deak D S 2013 Strontium titanate surfaces *Mater. Sci. Technol.* **23** 127–36

[26] Bonnell D A and Garra J 2008 Scanning probe microscopy of oxide surfaces: atomic structure and properties *Rep. Prog. Phys.* **71** 044501

[27] Szot K, Speier W, Carius R, Zastrow U and Beyer W 2002 Localized metallic conductivity and self-healing during thermal reduction of $SrTiO_3$ *Phys. Rev. Lett.* **88** 075508

[28] Islam M 2002 Computer modelling of defects and transport in perovskite oxides *Solid State Ion.* **154-55** 75–85

[29] Szot K and Speier W 1999 Surfaces of reduced and oxidized $SrTiO_3$ from atomic force microscopy *Phys. Rev.* B **60** 5909–26

[30] Szot K, Pawelczyk M, Herion J, Freiburg C, Albers J, Waser R, Hulliger J, Kwapulinski J and Dec J 1996 Nature of the surface layer in ABO_3-type perovskites at elevated temperatures *Appl. Phys.* A **62** 335–43

[31] Kim K J *et al* 2019 Facet-dependent *in situ* growth of nanoparticles in epitaxial thin films: the role of interfacial energy *J. Am. Chem. Soc.* **141** 7509–17

[32] Zhu T, Troiani H E, Mogni L V, Han M and Barnett S A 2018 Ni-substituted Sr(Ti,Fe) O_3 SOFC anodes: achieving high performance via metal alloy nanoparticle exsolution *Joule* **2** 478–96

[33] He S, Li M, Hui J and Yue X 2021 In-situ construction of ceria-metal/titanate heterostructure with controllable architectures for efficient fuel electrochemical conversion *Appl. Catal.* B **298** 120588–99

[34] Lv H *et al* 2021 Promoting exsolution of RuFe alloy nanoparticles on $Sr_2Fe_{1.4}Ru_{0.1}Mo_{0.5}O_{6-\Delta}$ via repeated redox manipulations for CO_2 electrolysis *Nat. Commun.* **12** 5665

[35] Jo S, Jeong H G, Kim Y H, Neagu D and Myung J-h 2021 Stability and activity controls of Cu nanoparticles for high-performance solid oxide fuel cells *Appl. Catal.* B **285** 119828

[36] Fan W, Sun Z and Bai Y 2022 Manipulating electrocatalytic activity of perovskite oxide through electrochemical treatment *Small* **18** e2107131

[37] Chen Z *et al* 2020 Organic photochemistry-assisted nanoparticle segregation on perovskites *Cell Rep. Phys. Sci.* **1** 4618

[38] Sun Y F, Zhang Y Q, Chen J, Li J H, Zhu Y T, Zeng Y M, Amirkhiz B S, Li J, Hua B and Luo J L 2016 New opportunity for *in situ* exsolution of metallic nanoparticles on perovskite parent *Nano Lett.* **16** 5303–9

[39] Tsekouras G, Neagu D and Irvine J T S 2013 Step-change in high temperature steam electrolysis performance of perovskite oxide cathodes with exsolution of *B*-site dopants *Energy Environ. Sci.* **6** 256–66

[40] Liu S, Liu Q and Luo J-L 2016 Highly stable and efficient catalyst with *in situ* exsolved Fe–Ni alloy nanospheres socketed on an oxygen deficient perovskite for direct CO_2 electrolysis *ACS Catal.* **6** 6219–28

[41] Yang C, Li J, Lin Y, Liu J, Chen F and Liu M 2015 In situ fabrication of CoFe alloy nanoparticles structured $(Pr_{0.4}Sr_{0.6})_3(Fe_{0.85}Nb_{0.15})_2O_7$ ceramic anode for direct hydrocarbon solid oxide fuel cells *Nano Energy* **11** 704–10

[42] Lai K-Y and Manthiram A 2018 Self-regenerating Co–Fe nanoparticles on perovskite oxides as a hydrocarbon fuel oxidation catalyst in solid oxide fuel cells *Chem. Mater.* **30** 2515–25

[43] Zhou N, Yin Y-M, Chen Z, Song Y, Yin J, Zhou D and Ma Z-F 2018 A Regenerative coking and sulfur resistant composite anode with cu exsolution for intermediate temperature solid oxide fuel cells *J. Electrochem. Soc.* **165** F629–34

[44] Kang B, Matsuda J and Ishihara T 2019 Cu–Fe–Ni nano alloy particles obtained by exsolution from $Cu(Ni)Fe_2O_4$ as active anode for SOFCs *J. Mater. Chem.* A **7** 26105–15

[45] Kousi K, Tang C, Metcalfe I S and Neagu D 2021 Emergence and future of exsolved materials *Small* **17** 2006479–505

[46] Tang C, Kousi K, Neagu D and Metcalfe I S 2021 Trends and prospects of bimetallic exsolution *Chemistry* **27** 6666–75

[47] Sengodan S, Ju Y-W, Kwon O, Jun A, Jeong H Y, Ishihara T, Shin J and Kim G 2017 Self-decorated MnO nanoparticles on double perovskite solid oxide fuel cell anode by *in situ* exsolution *ACS Sustain. Chem. Eng.* **5** 9207–13

[48] Zhao J, Pu Y, Li L, Zhou W and Guo Y 2020 Efficient ferrite-based perovskite anode for solid oxide fuel cells with *A*-site and *B*-site co-exsolution *Energy Fuels* **34** 10100–8

[49] Li B, He S, Li J, Yue X, Irvine J T S, Xie D, Ni J and Ni C 2020 A Ce/Ru co-doped $SrFeO_{3-\Delta}$ perovskite for a coke-resistant anode of a symmetrical solid oxide fuel cell *ACS Catal.* **10** 14398–409

[50] Wang W, Gan L, Lemmon J P, Chen F, Irvine J T S and Xie K 2019 Enhanced carbon dioxide electrolysis at redox manipulated interfaces *Nat. Commun.* **10** 1550

[51] Neagu D *et al* 2019 In situ observation of nanoparticle exsolution from perovskite oxides: from atomic scale mechanistic insight to nanostructure tailoring *ACS Nano* **13** 12996–3005

[52] Opitz A K *et al* 2017 Surface chemistry of perovskite-type electrodes during high temperature co$_2$ electrolysis investigated by operando photoelectron spectroscopy *ACS Appl. Mater. Interfaces* **9** 35847–60

[53] Opitz A K *et al* 2020 Understanding electrochemical switchability of perovskite-type exsolution catalysts *Nat. Commun.* **11** 4801

[54] Yu Y, Mao B, Geller A, Chang R, Gaskell K, Liu Z and Eichhorn B W 2014 CO_2 activation and carbonate intermediates: an operando AP-XPS study of CO_2 electrolysis reactions on solid oxide electrochemical cells *Phys. Chem. Chem. Phys.* **16** 11633–9

[55] Kim K, Joo S, Huang R, Kim H J, Kim G and Han J W 2021 Mechanistic insights into the phase transition and metal ex-solution phenomena of $Pr_{0.5}Ba_{0.5}Mn_{0.85}Co_{0.15}O_{3-\Delta}$ from simple to layered perovskite under reducing conditions and enhanced catalytic activity *Energy Environ. Sci.* **14** 873–82